

## Analysis of hydrodynamic trapping interactions during full-cycle injection and migration of CO<sub>2</sub> in deep saline aquifers

Wang, Y.; Vuik, Cornelis; Hajibeygi, H.

**DOI**

[10.1016/j.advwatres.2021.104073](https://doi.org/10.1016/j.advwatres.2021.104073)

**Publication date**

2022

**Document Version**

Final published version

**Published in**

Advances in Water Resources

**Citation (APA)**

Wang, Y., Vuik, C., & Hajibeygi, H. (2022). Analysis of hydrodynamic trapping interactions during full-cycle injection and migration of CO<sub>2</sub> in deep saline aquifers. *Advances in Water Resources*, 159, Article 104073. <https://doi.org/10.1016/j.advwatres.2021.104073>

**Important note**

To cite this publication, please use the final published version (if applicable). Please check the document version above.

**Copyright**

Other than for strictly personal use, it is not permitted to download, forward or distribute the text or part of it, without the consent of the author(s) and/or copyright holder(s), unless the work is under an open content license such as Creative Commons.

**Takedown policy**

Please contact us and provide details if you believe this document breaches copyrights. We will remove access to the work immediately and investigate your claim.



# Analysis of hydrodynamic trapping interactions during full-cycle injection and migration of CO<sub>2</sub> in deep saline aquifers

Yuhang Wang<sup>a,b,\*</sup>, Cornelis Vuik<sup>a</sup>, Hadi Hajibeygi<sup>b</sup>

<sup>a</sup> Faculty of Electrical Engineering, Mathematics and Computer Science, Department of Applied Mathematics, Delft University of Technology, Van Mourik Broekmanweg 6, 2628 XE Delft, The Netherlands

<sup>b</sup> Faculty of Civil Engineering and Geosciences, Department of Geoscience and Engineering, Delft University of Technology, Stevinweg 1, 2628CV, Delft, The Netherlands

## ARTICLE INFO

### Keywords:

Geologic carbon storage  
Multiphase flow in porous media  
Compositional simulation  
Multiphysics interaction

## ABSTRACT

CO<sub>2</sub> injection into deep saline aquifers has shown to be a feasible option, as for their large storage capacity under safe operational conditions. Previous studies have revealed that CO<sub>2</sub> can be trapped in the subsurface by several mechanisms. Despite the major advances in studying these trapping mechanisms, their dynamic interactions in different periods of a full-cycle process have not been well understood; i.e., they are studied independently at their so-called 'separate time scales of importance'. These mechanisms, however, are dynamically interconnected and influence each other even outside of their main time scale of importance. Besides, previous studies on field-scale simulations often choose grid cells which are too coarse to capture flow dynamics especially in post-injection period. To this end, we develop a comprehensive framework to analyze the flow dynamics and the associated hydrodynamic trapping process, in which the CO<sub>2</sub> injection, migration and post-migration period are all considered in a unified manner. Through illustrative models with sufficient grid resolution, we quantify the impact of different trapping mechanisms and uncertain reservoir properties through a full-cycle process. We demonstrate that the time scale associated with each trapping mechanism indeed varies, yet their dynamic interplay needs to be considered for accurate and reliable predictions. Results reveal that residual trapping is governed by the advective transport in the injection period, and its contribution to the overall trapped amount becomes more significant in systems with lower permeability. Dissolution trapping operates under varying driving forces at different stages. In the injection period, the dissolution process is controlled by advective transport, and later enhanced by the gravity-induced convection in the post-injection period. Such convective transport diminishes the contribution from residual trapping. Our study sheds light on the impact of the coupled reservoir and fluid time-dependent interactions in estimation of the securely trapped CO<sub>2</sub> in saline aquifers.

## 1. Introduction

Carbon dioxide capture and storage (CCS) has been identified as a promising strategy to mitigate climate change due to anthropogenic CO<sub>2</sub> emissions. Given the urgency with respect to limiting global warming, recent decades have witnessed a remarkable increase of research interest around CO<sub>2</sub> storage in subsurface systems (Bui et al., 2018). Of the geological media being considered, hydrocarbon (oil and gas) reservoirs and deep saline aquifers have shown to be successful at pilot and commercial scales (Orr Jr., 2009; Szulczewski et al., 2012; Bachu, 2015). Storing CO<sub>2</sub> in hydrocarbon reservoirs is relatively straightforward, because the geological structures in which buoyant hydrocarbons were retained for quite a long time have proved to be

safe. In addition, the storage capacity could be estimated based on the volume of produced oil/gas assuming hydrocarbons will be completely replaced by CO<sub>2</sub> (Bachu et al., 2007). The storage can become more economically attractive by being combined with enhanced oil recovery (EOR) (Dai et al., 2014; Ampomah et al., 2017) or geothermal energy production (Randolph and Saar, 2011). On the other hand, for CO<sub>2</sub> storage in saline aquifers, the flowing fluids are primarily composed of CO<sub>2</sub> and brine. Due to their distinct mobility contrast and geological heterogeneities, such a displacement process is unstable. Moreover, various trapping mechanisms operating on different time scales add to the complexity in understanding such a dynamic process.

\* Corresponding author at: Faculty of Civil Engineering and Geosciences, Department of Geoscience and Engineering, Delft University of Technology, Stevinweg 1, 2628CV, Delft, The Netherlands.

E-mail addresses: [Y.Wang-25@tudelft.nl](mailto:Y.Wang-25@tudelft.nl) (Y. Wang), [c.vuik@tudelft.nl](mailto:c.vuik@tudelft.nl) (C. Vuik), [h.hajibeygi@tudelft.nl](mailto:h.hajibeygi@tudelft.nl) (H. Hajibeygi).

<https://doi.org/10.1016/j.advwatres.2021.104073>

Received 2 July 2021; Received in revised form 5 October 2021; Accepted 26 October 2021

Available online 8 November 2021

0309-1708/© 2021 The Authors. Published by Elsevier Ltd. This is an open access article under the CC BY license (<http://creativecommons.org/licenses/by/4.0/>).

Mechanisms by which CO<sub>2</sub> can be retained in saline aquifers have been classified (Rubin and De Coninck, 2005), and include the following: (a) Structural and stratigraphic trapping, (b) residual trapping, (c) dissolution trapping, and (d) mineral trapping.

(a) Structural and stratigraphic trapping. This refers to the process of upward migration of buoyant CO<sub>2</sub> being inhibited by an overlying, impermeable (or low-permeable) cap rock. In such a case the risk of leakage is not eliminated because the accumulated CO<sub>2</sub> under the sealing rock is mobile. In practice, injection operations may overpressurize the reservoir, leading to activation of faults and fractures from which mobile CO<sub>2</sub> is likely to escape (Rutqvist, 2012; Zoback and Gorelick, 2012; Rinaldi et al., 2014; White et al., 2014; Espinoza and Santamarina, 2017; Zappone et al., 2021). This coupled process of fluid flow and geomechanics associated with CCS has attracted growing attention from both numerical and experimental perspectives, which is out of the scope of this work.

(b) Residual trapping. CO<sub>2</sub> is generally the non-wetting phase in many sedimentary rocks. Consequently, brine, as the wetting phase, tends to imbibe into CO<sub>2</sub> plume at the trailing edge after injection stops (Juanes et al., 2006). Such imbibition leaves CO<sub>2</sub> behind as disconnected immobile bubbles and ganglia (Hunt et al., 1988). This process is referred to as residual trapping. It originates from hysteresis which occurs when the rock exhibits strong wettability preference to a specific phase. Experimental investigations have revealed the hysteretic behavior of CO<sub>2</sub>-brine system by measuring relative permeability (Akbarabadi and Piri, 2013; Ruprecht et al., 2014), and capillary pressure (Wang and Tokunaga, 2015; Pini and Benson, 2017), as functions of saturation. These physical measurements demonstrate that constitutive relations rely on the history of saturation. As a consequence, the residual saturation of nonwetting phase is closely related to the history as well. To describe the trapping characteristics, several mathematical models have been developed. Prominent examples include the Land equation (Land, 1968) and the more recently proposed linear model (Steffy et al., 1997).

(c) Dissolution Trapping. Dissolution occurs as CO<sub>2</sub> contacts the undersaturated brine. Brine with dissolved CO<sub>2</sub> becomes more dense, and tends to sink rather than rising up; so the dissolved CO<sub>2</sub> is less susceptible to leakage. The amount of CO<sub>2</sub> which can dissolve into brine depends on several physical parameters, including pressure, temperature, and salinity of brine. The CO<sub>2</sub>-brine (or CO<sub>2</sub>-H<sub>2</sub>O) equilibrium phenomenon has been studied extensively from experimental perspective; the solubility of CO<sub>2</sub> in brine (or H<sub>2</sub>O) is measured across a wide range of temperatures and pressures, as summarized in literature (Diamond and Akinfiev, 2003; Duan and Sun, 2003; Spycher et al., 2003). These experimental data served as benchmarks for developing correlations or modifying the equation of state, such that mathematical models are capable of representing physical observations (Enick and Klara, 1990; Battistelli et al., 1997; Spycher et al., 2003; Li et al., 2011a). Note that transport of dissolved CO<sub>2</sub> is governed not only by convection, but also by hydrodynamic dispersion (Bear, 2013). The latter one is composed of molecular diffusion and mechanical dispersion. Molecular diffusion is driven by the concentration gradient, which is independent of the fluid flow. For a typical CO<sub>2</sub> diffusivity ( $\sim 10^{-9}$  m/s), the characteristic diffusion length is relatively small compared to the CO<sub>2</sub> plume dimension. Hence, molecular diffusion is usually not considered in field-scale simulations (Doughty, 2010). On the other hand, mechanical dispersion is induced by local velocity variations due to microscopic heterogeneity of the porous medium (Saffman, 1959; Bachmat and Bear, 1964). As such, this process is controlled by both fluid velocity and rock properties (e.g., porosity and tortuosity). The effect of hydrodynamic dispersion on convection is recently studied using high-resolution numerical simulations (Wen et al., 2018; De Paoli, 2021). Results reveal that the relative importance of the role played by molecular diffusion and mechanical dispersion leads to a different dissolution rate. Nevertheless, the macroscopic (Darcy scale) description of hydrodynamic dispersion is still not clear, which is a subject of ongoing investigation (Dentz et al., 2018; Liang et al., 2018).

(d) Mineral Trapping. This trapping occurs when dissolved CO<sub>2</sub> reacts with minerals of the reservoir rock: CO<sub>2</sub> could combine with H<sub>2</sub>O in liquid phase to form acid, i.e., carbonic acid (H<sub>2</sub>CO<sub>3</sub>), which leads to pH reduction and induces the dissolution/precipitation of minerals in the rock (Dai et al., 2020). Through chemical reactions CO<sub>2</sub> is trapped as a mineral phase, which can be retained for a long period of time (Matter and Kelemen, 2009). Despite its security, these interactions are affected by mineral compositions, and requires a detailed characterization of the mineral phases in the rock. Besides, owing to their extremely slow reaction rates, it may take thousands of years for reactions to reach equilibrium (Gaus, 2010). As a result, it poses significant challenges to model mineral trapping accurately.

Different trapping mechanisms operate on varying time scales. To clarify, we use the injection period as a reference. In general, structural and stratigraphic trapping, as well as residual trapping occur within the time scale close to the injection period, because they are controlled by advective transport. Dissolution trapping comes into play during the injection period as well, however, this trapping occurs over much longer time scale, and is considered to be the dominant trapping mechanism in the post injection period. Mineral trapping is retarded by slow reaction kinetics; its time scale may even be an order of magnitude larger than the dissolution trapping (Juanes et al., 2006). In addition, redsaline aquifers are often found in sandstone, which is a siliciclastic rock consisting of high percentage of quartz. This mineral makes an insignificant contribution to geochemical reactions through the trapping process (Gunter et al., 2000). Therefore, we will look into the first three trapping mechanisms in the following work. They are collectively referred to as hydrodynamic trapping (Bachu et al., 1994). Although mineral trapping is not considered, the time scale over which the other three trappings contribute still varies (Jiang, 2011). Moreover, integrating hydrodynamic trapping into a unique platform is a nontrivial task. Challenges include, but are not limited to, the aspects of: (a) Accurate description of thermodynamic properties of CO<sub>2</sub>-brine system, especially in presence of impurities. This directly affects the rate of CO<sub>2</sub> dissolution; (b) Robust algorithms to model hysteresis and its evolution in large-scale flow models as to quantify residual trapping; and (c) Development of efficient discretization methods and solvers that help to improve the numerical performance (Class et al., 2009; Celia et al., 2015; Bui et al., 2018).

Major advances in numerical modeling of CO<sub>2</sub>-brine systems have featured in: (a) simplified models with appropriate assumptions such that the computational complexity is reduced, and (b) fully-coupled models that include multiphase, multicomponent flow and transport. The vertical equilibrium model is a prominent example of the simplified ones (Nordbotten et al., 2005; Hesse et al., 2008; Dentz and Tartakovsky, 2009; Gasda et al., 2009; Guo et al., 2014; Tao et al., 2019). In this model, the pressure distribution is assumed to be in equilibrium in the 'vertical' direction orthogonal to the top and bottom boundaries, and phase segregation occurs quickly. As a result, profiles of the variables in the 'vertical' dimension are constructed using the solutions obtained in other dimension(s). This leads to the reduction of the problem size by one dimension. On the other side, the fully-coupled model relaxes these assumptions albeit at a larger computational expense in solving the coupled equations. One may investigate under which conditions a simplified model produces results that agree with such a fully-coupled one at a lower computational cost, and choose an effective simplified model to conduct more practical applications. For more information and discussion about different modeling approaches, readers are referred to Celia et al. (2015), Bandilla et al. (2015).

This work focuses on the fully-coupled model. In this scenario, depending on the purpose of each study, the trapping mechanism is often studied in an isolated manner. Examples include investigations of residual trapping (Juanes et al., 2006; Ide et al., 2007; Gershenson et al., 2017; Yang et al., 2020), and dissolution trapping (Hassanzadeh et al., 2007; Deng et al., 2012; Sathaye et al., 2014). Note that

hydrodynamic trapping has been included together in few research-grade or commercial simulators, e.g., TOUGH2 (Pruess et al., 1999) and CMG-GEM (Group, 2020). These simulators are employed to study CO<sub>2</sub> storage in large/field-scale saline aquifers. Impacts of various physical properties of rocks and fluids, including permeability, wettability, residual saturation, constitutive relations, as well as operational strategies on the amount to be trapped have been discussed extensively in literature (Doughty, 2010; Han et al., 2011; Li et al., 2011b; Wriedt et al., 2014; Manceau and Rohmer, 2016; Rasmusson et al., 2016; Al-Khdheawi et al., 2017; Jayne et al., 2019; Ershadnia et al., 2021). These investigations lend insight into determining the governing parameters under different situations. However, they suffer from two main limitations. First, due to a relatively coarse mesh size used in the studies, the gravity-induced convective transport, which plays an essential role in post-injection period, may not be fully captured. This could lead to an inaccurate assessment of the trapped amount especially for dissolution trapping. Secondly, such sensitivity/uncertainty analysis are often conducted based on the trapped amount obtained at a single point in time (end of the simulation). As a consequence, the dynamic behavior of fluid flow in a highly unstable multiphase system, and its impact on different trapping mechanisms remain relatively unexplored. It is worth mentioning that several studies have been conducted to compare modeling results from different research teams (Class et al., 2009; Nordbotten et al., 2012). They identified possible sources of differences observed in the results, and highlighted several aspects which merit attention: (a) A grid convergence study is of importance to minimize the grid induced errors; (b) A step-wise analysis should be conducted to investigate how model predictions react to different assumptions and simplifications; and (c) Meaningful predictions may only be possible with real-time monitoring and history matching techniques. Driven by these limitations and learnings from previous studies, in this work we analyze the dynamics of such multicomponent, multiphase flow, and the associated interactions between different hydrodynamic trapping mechanisms in a full-cycle period. The aforementioned model comparison studies have demonstrated that different assumptions lead to deviating prediction results, whereas the causes behind such deviations may not be well understood. To address this, we develop a numerical simulator to allow for the studying of the interactions of different trapping mechanisms in a fully coupled system. The underlying physics of different trapping mechanisms are modeled in one workflow.

In the remainder of this paper, we first present governing equations and essential physical models involved in CO<sub>2</sub> storage in saline aquifers. Details of the physics associated with residual and dissolution trapping are addressed. We then validate the developed simulator against a theoretical model reported in literature, followed by a grid convergence test. Next, we discuss the results obtained from different scenarios. Time-lapsed gas saturation and solution CO<sub>2</sub>-brine ratio profiles are visualized at representative points in time. In addition, contributions from different trapping mechanisms are quantified and analyzed. We close with the key findings of this work.

## 2. Physical models and methods

### 2.1. Governing equations

We employ generalized mass conservation equations to describe the multicomponent, multiphase system. Specifically, two phases are present, i.e., gas and liquid, which are composed of two components: CO<sub>2</sub> and brine. Brine consists of H<sub>2</sub>O and dissolved salt. The governing equations are given by:

$$\frac{\partial}{\partial t} \left( \phi \sum_{\alpha} x_{c,\alpha} \rho_{\alpha} S_{\alpha} \right) + \nabla \cdot \left( \sum_{\alpha} x_{c,\alpha} \rho_{\alpha} \mathbf{u}_{\alpha} \right) - \sum_{\alpha} x_{c,\alpha} q_{\alpha} = 0, \quad (2.1)$$

where the subscripts  $\alpha$  and  $c$  denote the phases ( $l$  and  $g$  for liquid and gas) and components (CO<sub>2</sub> and brine), respectively.  $\phi$  is the porosity of porous medium,  $\rho_{\alpha}$ ,  $S_{\alpha}$ , and  $q_{\alpha}$  are density, saturation and source term

of phase  $\alpha$ .  $x_{c,\alpha}$  is the mole (mass) fraction of component  $c$  in phase  $\alpha$ .  $\mathbf{u}_{\alpha}$  is Darcy velocity expressed as

$$\mathbf{u}_{\alpha} = -\frac{k k_{r\alpha}}{\mu_{\alpha}} \nabla \psi_{\alpha}, \quad (2.2)$$

where  $k$  is rock permeability,  $k_{r\alpha}$ ,  $\mu_{\alpha}$ , and  $\psi_{\alpha}$  are relative permeability, viscosity, and potential of phase  $\alpha$ .  $\psi_{\alpha}$  is given by

$$\psi_{\alpha} = p_{\alpha} - \rho_{\alpha} g h, \quad (2.3)$$

where  $g$  is gravitational acceleration and  $h$  is depth. Phase pressures are related to each other by capillary pressure,  $P_c$ .

The overall-composition variable set is used (Voskov and Tchelepi, 2012; Cusini et al., 2018). In general, for a system of  $m$  components, this formulation uses one phase pressure (e.g., pressure of the wetting phase denoted by  $p_w$ ) and  $(m-1)$  total mole fractions ( $z_c$ ) as primary variables. The residuals of  $m$  governing equations are linearized with respect to primary variables given by

$$r_c^{v+1} \approx r_c^v + \frac{\partial r_c}{\partial p_w} \Big|_v \delta p_w^{v+1} + \sum_{i=1}^{m-1} \frac{\partial r_c}{\partial z_i} \Big|_v \delta z_i^{v+1} = 0, \quad (2.4)$$

where  $v$  and  $v+1$  are iteration steps. Here we have two components and two phases, in which the liquid phase pressure ( $p_l$ ) and CO<sub>2</sub> mole fraction ( $z_{\text{CO}_2}$ ) serve as primary variables. The coupled system is solved using a fully implicit scheme (Aziz, 1979; Cusini et al., 2018).

### 2.2. Dissolution trapping

The amount of CO<sub>2</sub> present in the liquid phase is quantified via the solution CO<sub>2</sub>-brine ratio,  $R_s$ , defined as the volume of CO<sub>2</sub> which dissolves into unit volume of brine at a given condition. Based on the measured CO<sub>2</sub> solubility across various conditions, thermodynamic models tailored to the CO<sub>2</sub>-brine system have been developed in literature. We follow the thermodynamic model based on equating chemical potentials to predict the solubility of CO<sub>2</sub> at a given temperature and salinity (Spycher et al., 2003). For detailed procedures, readers are referred to Appendix. The resulting relation between  $R_s$  and  $x_{\text{CO}_2,l}$  is given by Hassanzadeh et al. (2008)

$$R_s = \frac{\rho_b^{\text{STC}} x_{\text{CO}_2,l}}{\rho_{\text{CO}_2}^{\text{STC}} (1 - x_{\text{CO}_2,l})}, \quad (2.5)$$

where the subscript 'b' is short for brine, the superscript 'STC' denotes a property at standard conditions.

To verify our implementation, the calculated molality curves of CO<sub>2</sub> in liquid phase at 60°C are compared with the data reported in literature (Spycher and Pruess, 2005). As shown in Fig. 1A, predictions from the module agree well with the reference data across various salinity values which are typical in saline aquifers. The molality data are then converted into solution CO<sub>2</sub>-brine ratios using Eq. (2.5), and results are presented in Fig. 1B. We observe that at the given temperature and salinity,  $R_s$  depends on pressure only. These curves are eventually translated into lookup tables in the flow simulation.

Physically speaking, in each cell the amount of CO<sub>2</sub> that can dissolve into brine cannot exceed the available CO<sub>2</sub>. Therefore, it is important to identify the number of existing phases (Hajibeygi and Tchelepi, 2014). To do that, a stability check is performed after updating primary variables in each iteration step. For this two-phase isothermal system, the fluid of a cell is in a single liquid phase if

$$\sum_c z_c K_c - 1 < 0, \quad (2.6)$$

is satisfied Danesh (1998), where  $K_c$  is the equilibrium ratio (known as  $K$ -values) expressed as

$$K_c = \frac{x_{c,g}}{x_{c,l}}. \quad (2.7)$$

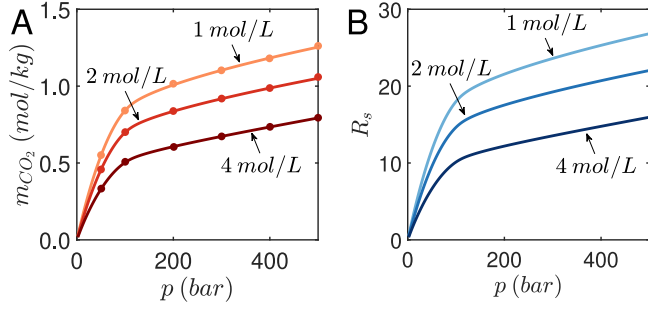


**Fig. 1.** Predicted solubilities of CO<sub>2</sub> in brine at 60°C. (A) Verification of the thermodynamic model implemented in this work. Results (represented by solid curves) are compared against the reference data (represented by circles) obtained using the full solubility model (Duan and Sun, 2003). (B) Solution CO<sub>2</sub>-brine ratio curves at different salinities.

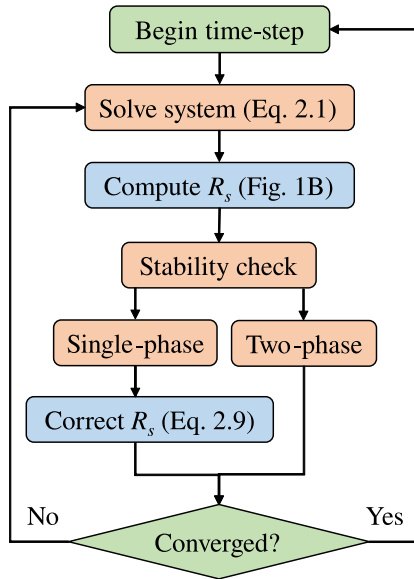


**Fig. 2.** Workflow for calculation of dissolved CO<sub>2</sub>.

For the fluid model considered in this work,  $K$ -values for CO<sub>2</sub> and brine are given by

$$K_{\text{CO}_2} = \frac{\rho_{\text{CO}_2}^{\text{STC}} R_s + \rho_{\text{b}}^{\text{STC}}}{\rho_{\text{CO}_2}^{\text{STC}} R_s}, \text{ and } K_{\text{b}} = 0. \quad (2.8)$$

If the current cell is in two-phase state, the amount of dissolved CO<sub>2</sub> is obtained from solution CO<sub>2</sub>-brine ratio curve, which is generated in an offline stage (The solution ratio curve is calculated using an independent (i.e., offline) module before the simulation starts.) On the other hand, if the cell is in undersaturated state, i.e., only the liquid phase exists,  $R_s$  is calculated based on mole fractions of the CO<sub>2</sub> component:

$$R_s = \frac{\rho_{\text{b}}^{\text{STC}} z_{\text{CO}_2}}{\rho_{\text{CO}_2}^{\text{STC}} (1 - z_{\text{CO}_2})}. \quad (2.9)$$

In both scenarios the governing equation is well posed, and the workflow associated with calculation of dissolved CO<sub>2</sub> is summarized in Fig. 2.

### 2.3. Residual trapping

Here we discuss the hysteretic behavior of the constitutive relations, which are critical for secure CO<sub>2</sub> trapping after injection ceases. In general, relative permeability and capillary pressure functions are known as constitutive relations; they govern the interactions between wetting (liquid) and nonwetting (gas) phases, and also reflect the transport property of the matrix. The non-hysteretic model takes constitutive relations as functions of current local saturation only, whereas the hysteretic model depends on not only current local saturation, but also the history of saturation. To illustrate, Figs. 3A and 3B show constitutive relations used in the simulation. The relative permeability curves approximate the experimental data reported in literature (Oak et al., 1990) using a van Genuchten equation (van Genuchten, 1980). The experiment was conducted using Berea sandstone which is strongly water wet, and therefore, we observe that the hysteresis effect is pronounced for the nonwetting gas phase, whereas the wetting phase follows almost the same curve in both drainage and imbibition processes. Capillary pressure curves are given in the form of the Leverett  $J$ -function. These curves of constitutive relations are believed to be representative of a CO<sub>2</sub>-brine system (Ruprecht et al., 2014; Kuo and Benson, 2015; Abdoulghafour et al., 2020). Note that predictions of such dynamic process are affected by the choice of models describing constitutive relations (Court et al., 2012; Oostrom et al., 2016); their impacts are beyond the scope of this work.

To mimic the initial conditions, we assume the gas saturation is at its minimum, i.e.,  $S_g = 0$ . As CO<sub>2</sub> starts being pumped into the reservoir, constitutive relations follow the primary drainage curves until  $S_g$  reaches the maximum gas saturation,  $S_{g,\text{max}}$ . If  $S_g$  starts decreasing after reaching this point, constitutive relations will travel along the primary imbibition curve until  $S_g$  reduces to the residual gas saturation,  $S_{gr}$  ( $S_{g,\text{max}}$ ). However, if drainage is interrupted before  $S_g$  reaches  $S_{g,\text{max}}$ , which is often the case, the process is then transitioned from drainage to imbibition along the scanning curve, which is created to ensure the transition is continuous (Killough, 1976; Carlson, 1981; Plohr et al., 2001). The scanning curve is obtained based on the primary drainage and imbibition curves, referred to as bounding curves (Killough, 1976). The point where the transition occurs is named turning point ( $S_{gt}$ ), and its corresponding residual saturation ( $S_{gr}$  ( $S_{gt}$ )) is determined using a linear trapping model (Steffy et al., 1997):

$$S_{gr} = f_r S_{gt}, \quad (2.10)$$

where  $f_r$  is a constant fraction. This relation indicates that the trapped gas saturation increases along with the turning point saturation. It is worth mentioning that when flow occurs along a scanning curve, i.e.,  $S_{gr}$  ( $S_{gt}$ )  $<$   $S_g$   $<$   $S_{gt}$ , any alternation of the flow processes will not produce a new scanning curve for the sake of numerical stability.

The main steps of computing the hysteretic constitutive relations are presented in Algorithm 1, with a focus on the situation in which the transition happens. As shown, this algorithm entails a comparison of gas saturation ( $S_g$ ) at previous two time steps, i.e.,  $n$  and  $(n - 1)$ , along with a boolean parameter,  $\mathcal{L}_{sc}$ . Here  $\mathcal{L}_{sc}$  is nonzero if the flow process follows a scanning curve, otherwise its value is zero. It is used to keep track of the history of flow process. In addition, this algorithm requires the turning point at time step  $n$  ( $S_{gt}^n$ ) in order to determine when the process leaves a scanning curve and returns to the drainage bounding curve.  $\mathcal{L}_{sc}$  is updated whenever a transition occurs. Because each cell has its own saturation history, the turning point differs from cell to cell. This leads to different scanning curves as shown in Figs. 3B and 4B.

### 2.4. Simulator validation & setup

#### 2.4.1. Validation

We first validate the developed simulator against the solution of a theoretical model. We consider the instantaneous release of buoyant

**Algorithm 1:** Computation of hysteretic constitutive relations.

```

Input:  $L_{sc}^n, S_g^n, S_g^{n-1}, S_{gt}^n$ 
Output:  $k_{rg}^{n+1}, P_c^{n+1}$ 
/* Transition from drainage bounding curve to scanning
curve */
1 if  $(\sim L_{sc}^n) \& (S_g^n < S_g^{n-1})$  then
2    $S_{gt}^{n+1} \leftarrow S_g^{n-1}$ 
3    $k_{rg}^{n+1} \leftarrow k_{rg}^{i,n+1}(S_{gt}^{n+1}, S_g^{n+1})$ 
4    $P_c^{n+1} \leftarrow P_c^{i,n+1}(S_{gt}^{n+1}, S_g^{n+1})$ 
5    $L_{sc}^{n+1} \leftarrow 1$ 
/* Transition from scanning curve back to drainage
bounding curve */
6 else if  $L_{sc}^n \& (S_g^n > S_g^{n-1}) \& (S_g^n == S_{gt}^n)$  then
7    $S_{gt}^{n+1} \leftarrow S_{g,max}$ 
8    $k_{rg}^{n+1} \leftarrow k_{rg}^d(S_g^{n+1})$ 
9    $P_c^{n+1} \leftarrow P_c^d(S_g^{n+1})$ 
10   $L_{sc}^{n+1} \leftarrow 0$ 

```

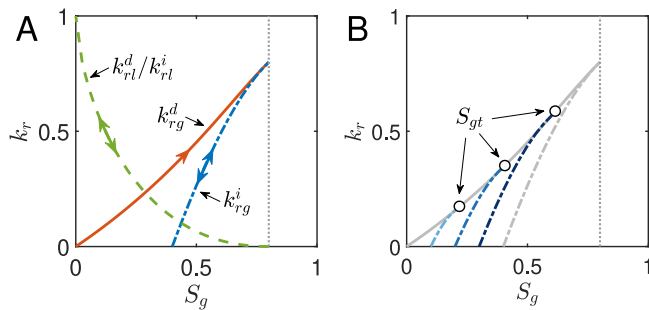


**Fig. 3.** Illustration of hysteretic behavior of relative permeability curves. (A) Primary drainage/imbibition curves for liquid and gas phases, where the superscript  $d$  and  $i$  denote drainage and imbibition, respectively. Single/Double head arrow indicates that the process along a given curve is irreversible/reversible, respectively. (B) Scanning curves generated at the turning point given by  $S_{gt} = 0.2, 0.4,$  and  $0.6$ .

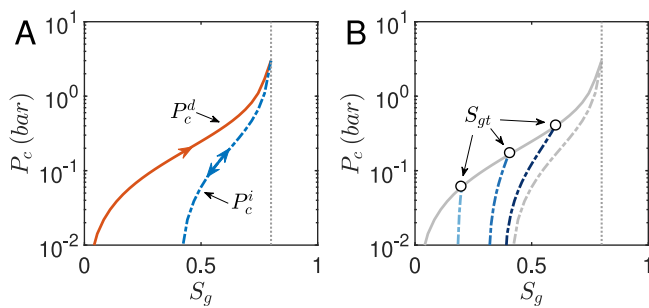


**Fig. 4.** Illustration of hysteretic behavior of capillary pressure curves. (A) Primary drainage/imbibition curves. (B) Scanning curves generated at the turning point given by  $S_{gt} = 0.2, 0.4,$  and  $0.6$ .

fluid (with fixed amount) into a horizontal aquifer in a two-dimensional domain (MacMinn et al., 2012). The buoyant fluid initially fills a small portion on the left side of the aquifer, and the ambient fluid with higher density occupies the rest pore volume. Capillary pressure and dissolution are excluded in the model. The spreading of buoyant fluid can be described using the following equation (Bear, 2013)

$$\frac{\partial h}{\partial t} - U \frac{\partial}{\partial x} \left[ (1-f)h \frac{\partial h}{\partial x} \right] = 0, \quad (2.11)$$

**Table 1**

Physical parameters used in the numerical simulation for the validation case.

Parameter	Value	Unit
Aquifer length	100	m
Aquifer height	20	m
Porosity	0.2	–
Absolute permeability	$1.0e-13$	$m^2$
Buoyant fluid density	900	$kg/m^3$
Ambient fluid density	1000	$kg/m^3$
Buoyant fluid viscosity	$1.0e-3$	Pa·s
Ambient fluid viscosity	$1.0e-3$	Pa·s
Initial Length of buoyant fluid	15	m

where  $h(x, t)$  is the depth of the buoyant current at a given location  $x$  and time  $t$ .  $U$  is the characteristic buoyancy velocity given by

$$U = \frac{\Delta \rho g k}{\phi \mu_l}, \quad (2.12)$$

where  $\Delta \rho = \rho_h - \rho_l$ , which denotes the density difference between ambient (heavy) fluid and buoyant (light) fluid (subscripts  $h$  and  $l$  are short for heavy and light fluid, respectively). The function  $f$  is given by

$$f = \frac{Mh}{(M-1)h + H}, \quad (2.13)$$

where  $M = \mu_h/\mu_l$  is the mobility ratio, and  $H$  is the height of the aquifer. The parameters used in the validation case is summarized in Table 1.

Fig. 5A presents the saturation maps of buoyant fluid at four moments. In each map, prediction of the depth of the buoyant current obtained from the theoretical model, i.e., Eq. (2.11), is delineated by the dashed line. As shown, simulation results capture the spreading of buoyant fluid predicted by the theoretical model. In addition, we compare the leading position of the buoyant current shown in Fig. 5B. Simulation results follow the forecast of the theoretical model satisfactorily.

#### 2.4.2. Setup

From a geological perspective, saline aquifers often have a dominating length in the longitudinal direction compared to their cross-sectional width. In such a case, a 2D representation may be sensible in order to study interactions of different trapping mechanisms. Here simulations are performed in a two-dimensional, vertical cross-section of a saline aquifer. The length and height of the aquifer are 100 m and 50 m, respectively, which is discretized by  $100 \times 50$  cells. A grid convergence test is performed in the following subsection.  $CO_2$  is injected at a constant rate ( $8 \times 10^{-5}$  pore volume per day) through the bottom 10 m of the domain on the left side. A production well penetrating the entire depth is placed on the right side. The injection lasts 600 days followed by shut in of both wells. We first consider a homogeneous permeability field ( $k = 40$ md) and investigate the dynamic interactions of different trapping mechanisms. This case is referred to as the base case, and the physical parameters used in the simulation are presented in Table 2. Values of these physical parameters, including pressure, temperature, and brine salinity are taken from the work conducted by Ide et al. (2007). They are believed to be typical for the sequestration of  $CO_2$  (being a supercritical fluid) in deep ( $\approx 2500$ m) saline aquifers. Such settings, however, do not apply for shallow aquifers where  $CO_2$  is in the gaseous phase.

Note that with the given physical parameters and the simulation settings, the resulting capillary number range (away from well-bore) is approximately 0 to  $10^{-7}$ , which is in line with the range reported by Ni et al. (2021) for field-scale scenarios. As a result, flow tends to fall in the capillary-dominated regime (Lenormand et al., 1988; Zhang et al., 2011; Guo and Aryana, 2019), in which the validity of the classical model (multiphase extension of Darcy's law, i.e., Eq. (2.2)) can be

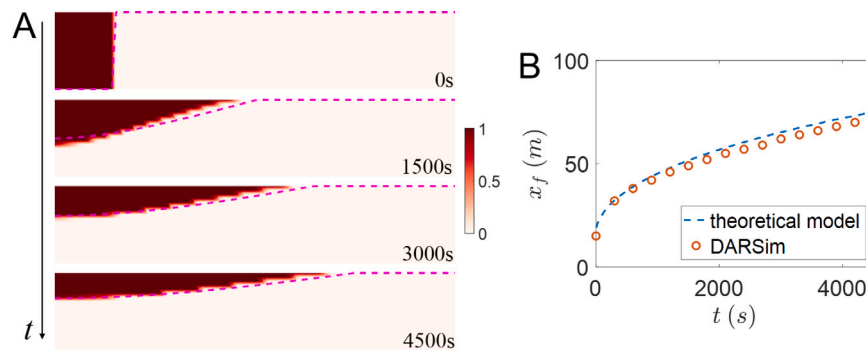


Fig. 5. (A) Saturation maps of the buoyant fluid obtained from numerical simulations, along with predictions of the theoretical model (dashed lines) at  $t = 0s, 1500s, 3000s,$  and  $4500s$ . (B) Leading position of the buoyant current obtained from numerical simulations (circles) and the theoretical model (dashed line).

**Table 2**  
Physical parameters and simulation settings for the base case. (ppm: parts per million; PV: pore volume.)

Parameter	Value	Unit
Aquifer length	100	m
Aquifer height	50	m
Porosity	0.2	–
Absolute permeability	$4.0e-14$	$m^2$
Initial pressure	$2.5e7$	Pa
Bottom hole pressure	$2.5e7$	Pa
Temperature	338.15	K
CO <sub>2</sub> density at STC	1.98	kg/m <sup>3</sup>
Brine salinity	$1.0e5$	ppm
Brine density at STC	1060	kg/m <sup>3</sup>
Injection rate	$8.0e-5$	PV/day
Simulation time	$3.6e4$	day
Injection time	$6.0e2$	day

**Table 3**  
Simulation cases and their differences compared to the base case.

Case	Label	Comments (compared to the base case)
1	'base'	–
2	'no hysteresis'	$k_r$ and $P_c$ follow primary drainage curves only.
3	'no capillarity'	$P_c = 0$ .
4	'no dissolution'	$R_s = 0$ .
5	'L = 50 m'	L is reduced from 100 m to 50 m.
6	'L = 200 m'	L is increased from 100 m to 200 m.
7	'k = 20 md'	k is reduced from 40 md to 20 md.
8	'k = 72 md'	k is increased from 40 md to 72 md.
9	'mSPE10Top'	k is heterogeneous with patchy pattern.
10	'mspe10Bottom'	k is heterogeneous with channeling pattern.

challenged. Alternatively, non-equilibrium models can be considered, as discussed in the literature (Hassanizadeh and Gray, 1993; Barenblatt et al., 2002; Joekar-Niasar et al., 2010; Wang et al., 2019). However, despite being widely used, it is not yet trivial to confirm whether or not the equilibrium-based model selected for this study is representative enough. Consideration of the impact of non-equilibrium physics stays outside the scope of this work, and can be performed in future research.

To demonstrate the relative significance of incorporating hysteresis, capillary pressure, and dissolution into the model, simulations are also conducted in the absence of these physics. Followed by that we look into the impacts of spatial heterogeneity by imposing nonhomogeneous permeability fields. In particular, we consider two cases modified from the top and bottom layer of SPE10 comparative test case (Christie and Blunt, 2001). They are labeled as 'mSPE10Top' and 'mSPE10Bottom', respectively. In both cases the permeability field is scaled such that the average permeability is the same as the permeability in the homogeneous case. All simulation cases discussed in the next section are summarized in Table 3, in which the difference of each case compared to the base one is commented upon.

### 2.4.3. Grid convergence

A grid convergence test is performed using physical parameters and simulation settings presented in Table 2. For simplicity, hysteresis is not considered in this test. As aforementioned, the gravity-induced convection in post-injection period triggers the development of sinking fingers from the top saturated layer. For this reason, capturing the evolution of descending fingers is essential for quantifying the amount of dissolution.

Simulations are performed at different resolutions with the grid size given by 5 m, 2 m, 1 m, and 0.5 m, in each direction. Fig. 6A shows the solution CO<sub>2</sub>-brine ratio (equivalent to CO<sub>2</sub> concentration) at the end of simulation. It is observed that as the mesh becomes finer, more details of the convection front are resolved: number of fingers increases in the map with a higher resolution. The time-lapsed behavior of trapping fraction, defined as the ratio of the trapped CO<sub>2</sub> over the total amount of injection, is presented in Fig. 6B. As shown, the result obtained when  $\delta x = 5m$  has relatively pronounced differences compared to the other curves. Moreover, the prediction from the case of  $\delta x = 1m$  agrees with that obtained when  $\delta x = 0.5m$ , except at intermediate times.

It should be noted that to fully resolve flow instability, the grid size is usually set to be below the critical wavelength (Riaz and Tchelepi, 2006; Berg and Ott, 2012; Fu et al., 2013; Hewitt et al., 2013; Green and Ennis-King, 2014; Wang et al., 2020; Pirozzoli et al., 2021). However, such resolution may not be practical for field-scale applications. Here the maps of the solution CO<sub>2</sub>-brine ratio do exhibit differing fingering behavior in cases when  $\delta x = 1m$  and  $\delta x = 0.5m$ , nevertheless, the time-lapsed dissolution rates seem to converge. At the end of the simulation period, the difference of the dissolved amount between the two cases is around 2%. This indicates that capturing each individual finger may not be necessary for the convergence of trapping quantities (Elenius et al., 2015). To balance the accuracy and computational cost, we use the grid size of  $\delta x = 1m$  in the following study. This grid resolution is also reported to be sufficient for relatively large-scale models in literature (Yamamoto and Doughty, 2011; Oostrom et al., 2016; Elenius et al., 2015; Wen and Benson, 2019; Lyu et al., 2021).

## 3. Results and discussion

Our main results exhibit the dynamics of interactions between CO<sub>2</sub> and brine in a full-cycle process, including CO<sub>2</sub> injection, migration, and post-migration periods. To provide quantitative comparisons in each simulated case, we record the amount of CO<sub>2</sub> trapped by dissolution and residual trapping, which are considered to be secure in hydrodynamic trapping. They are calculated based on the solution CO<sub>2</sub>-brine ratio and gas phase saturation maps, respectively. The overall trapped amount is the summation of these two types.

In the following discussion, the nondimensionalized elapsed time,  $t$ , defined as the ratio of the elapsed time over the duration of the

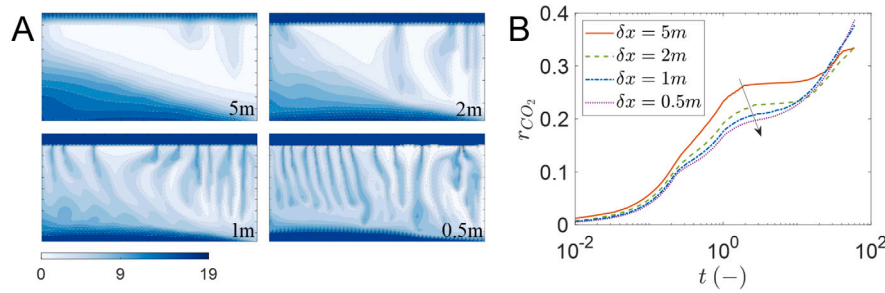


Fig. 6. (A) Solution CO<sub>2</sub>-brine ratio maps of different resolutions at the end of the simulation period. (B) Fraction of injected CO<sub>2</sub> trapped by dissolution obtained from cases of different resolutions. Elapsed time is nondimensionalized with respect to the duration of the injection period. The arrow indicates the direction in which the mesh is refined.

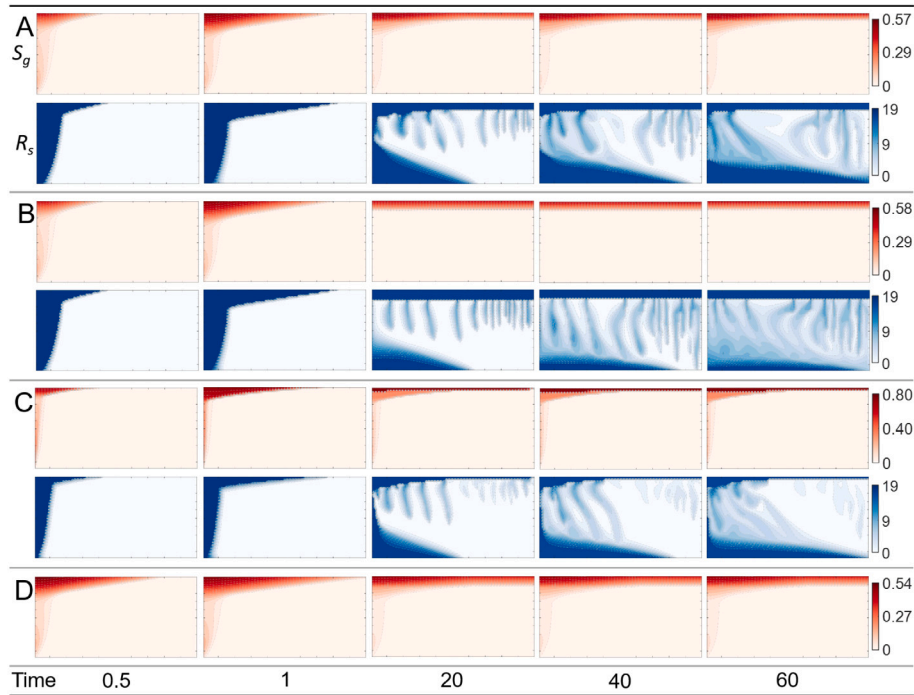


Fig. 7. Gas phase saturation and solution CO<sub>2</sub>-brine ratio profiles for various scenarios in a homogeneous permeability field. (A) shows results from the base case; (B), (C), and (D) present results from the case without hysteresis, capillary pressure, and dissolution, respectively. (D) includes saturation maps only because the solution ratio is zero at all times.

injection period, is used. This indicates the injection period is  $0 < t < 1$ , and injection ceases right at  $t = 1$ . The injected volume of CO<sub>2</sub> is 3% of the aquifer pore volume. In each case, the profile of  $S_g$  and  $R_s$  are visualized at five moments: one during injection period,  $t = 0.5$  (~0.8 years), one at the end of injection,  $t = 1$  (~1.6 years), and the remaining three in the post-injection period,  $t = 20, 40, 60$  (~ 32.9, 65.7, 98.6 years). Our results provide insight into the interplay of these trapping mechanisms and the underlying physics that were previously unexplored.

### 3.1. Temporal multiscale nature

The saturation and dissolution ratio profiles (shown in Fig. 7) clearly reveal the variety of time scales in which different trapping mechanisms operate. Take the base case as an example (shown in Fig. 7A). During the injection period, the evolution of saturation distribution is obvious: CO<sub>2</sub> flows upwards as soon as it is injected from the bottom layer due to strong buoyancy forces. After flow arrives at the top boundary, it develops in the horizontal direction underneath the sealing layer. In the post injection period, however, differences between saturation maps are insignificant. The saturation maps partially reveal the fraction of trapped CO<sub>2</sub> due to residual trapping. As

shown in Fig. 8B, the solid curve (in red) increases immediately after the injection ceases, reaching the maximum level in a short period of time ( $t \approx 2$ ). After that the fraction curve starts to decrease, which is not revealed in saturation maps. This is resulting from the interplay between different trapping mechanisms, which will be discussed in the following subsection.

As for  $R_s$ , we look into the solution ratio maps (of the base case for illustration as well). During the injection period, dissolution occurs along with the invasion of CO<sub>2</sub>: the contact interface in the profile of  $R_s$  evolves with that in the  $S_g$  map simultaneously. At this stage the amount of dissolved CO<sub>2</sub> is controlled by the advective transport. After the injection period, the CO<sub>2</sub> saturated region can be classified into two regions with different behaviors: The first region is formed by the vertical migration of CO<sub>2</sub>, and the second one is created by the lateral spreading underneath the top boundary. In the first region, the CO<sub>2</sub>-rich brine slumps away from the source region and propagates along the bottom layer. A transition zone is developed between the gravity current and the overriding brine. Meanwhile, in the second region, since the top saturated layer is more dense than the underlying intact brine, it is unstable and creates descending fingers rooted along the contact interface. Note that despite the mechanism of dissolution trapping varies temporally (during and after the injection period),

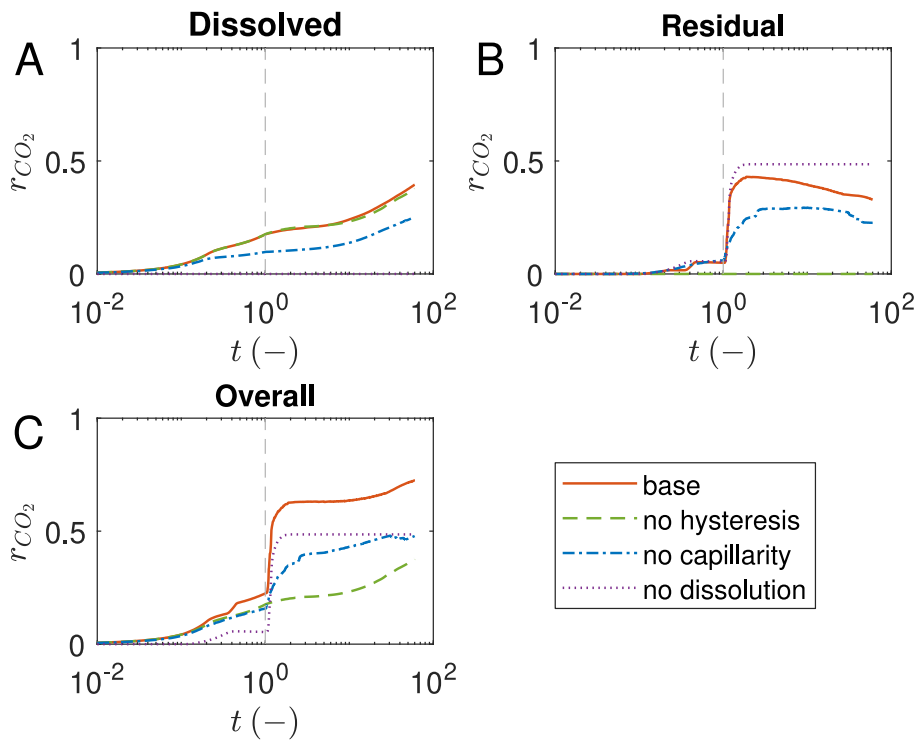


Fig. 8. Fraction of injected CO<sub>2</sub> trapped by different mechanisms in a homogeneous permeability field. The vertical dashed line indicates the moment at which injection ceases ( $t = 1$ ).

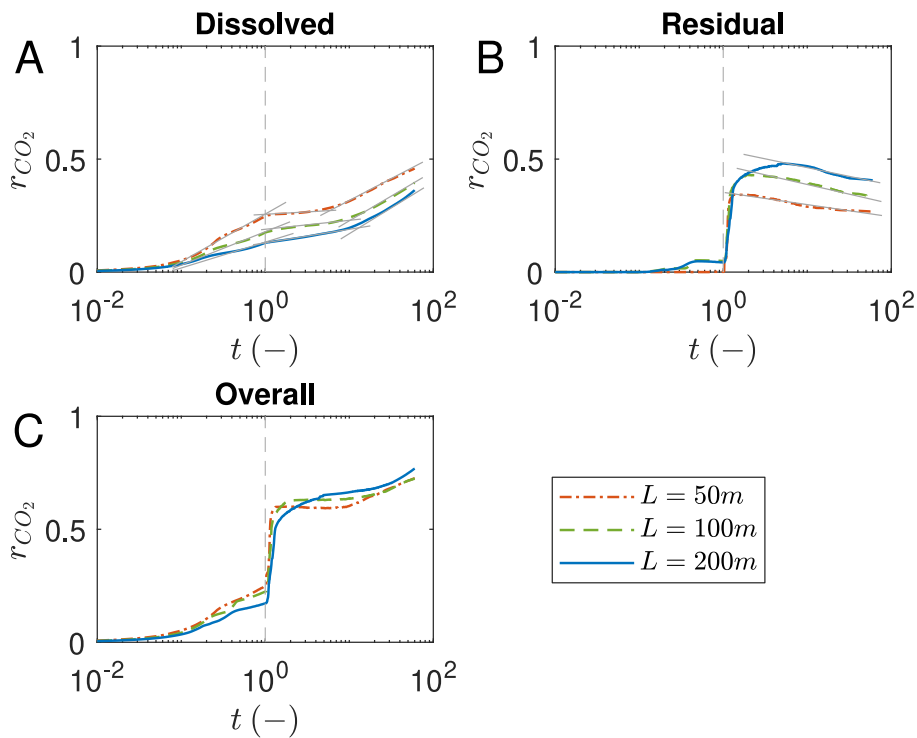


Fig. 9. Fraction of injected CO<sub>2</sub> trapped by different mechanisms in the sensitivity study. Solid lines depict transitions of different stages for dissolution trapping in (A), and the decline of residual trapping in post-injection period in (B). The vertical dashed line indicates the moment at which injection ceases ( $t = 1$ ).

its contribution seems to be equally important as shown in Fig. 8A. This implies that ignoring the dissolution trapping during the injection period may lead to an underestimate of the overall trapping amount.

To illustrate the impact of model scale on the dynamic behavior of trapping, we perform a sensitivity analysis by changing the length

of the aquifer. Two additional cases are considered with length of 50 m and 200 m. Physical parameters and well treatment are identical to that of the base case. Time-lapsed behaviors of different trapping mechanisms are presented in Fig. 9. As shown, fraction curves obtained

from different model scale follow similar patterns. Specifically, dissolution trapping has an observable growth during the injection period; its growth rate slows down after injection ceases and increases again at late time. Transitions of different stages are depicted by straight lines shown in Fig. 9A. As for residual trapping, its fraction increases rapidly right after the cease of injection followed by decline at a relatively small rate. Note that despite contributions from the two trapping mechanisms varying for models with different scales, the underlying physics, which govern their interactions through the investigated period, are equivalent. In other words, the trapping rates obtained from cases with varying aquifer length follow a similar pattern, as depicted by solid gray lines in Figs. 9A. and 9B. We will therefore focus our discussions on the model with the same size to that of base case.

### 3.2. Interplay of hysteresis and dissolution trapping

If hysteresis is not considered in the model, the constitutive relations are evaluated based on primary drainage/imbibition curves (shown in Fig. 3). In this case, residual saturation of gas phase becomes zero, and therefore, residual trapping is zero at all times (shown in Fig. 8B). As aforementioned, advective transport plays a major role during the injection period, and therefore, gas saturation increases monotonically in most, if not all, of the swept cells. Under such a process the impact of hysteresis is trivial. We observe that the  $S_g$  and  $R_s$  profiles in these two cases (with/without hysteresis) are almost identical, and their fraction curves for dissolved  $\text{CO}_2$  are overlapping (shown in Fig. 8A). After injection ceases,  $\text{CO}_2$  that remained near the injection well moves upwards and accumulates near the top of the aquifer. This leads to a thicker saturated layer compared to the base case, followed by the development of sinking fingers. We note that the interaction of fingers becomes more pronounced without hysteresis. The number of fingers is reduced observably near the production well from  $t = 20$  to  $t = 40$ : small scale fingers tend to merge at the finger root and develop into large scale fingers. Now that all free  $\text{CO}_2$  migrates upward, less will travel laterally with the gravity current as dissolved  $\text{CO}_2$ . Such a reduction in dissolved  $\text{CO}_2$  seems to be partially offset by a stronger fingering behavior which enhances the dissolution. As a result, the amount of dissolved  $\text{CO}_2$  without hysteresis is close to that of the base case throughout the full-cycle process.

Next we exclude dissolution by assuming  $\text{CO}_2$  exists in gas phase only. The resulting system becomes immiscible, and dissolution trapping vanishes accordingly. As shown in Fig. 7D, the front position of  $\text{CO}_2$  plume propagates further compared to that of the base case during the injection period. This is because the amount of free  $\text{CO}_2$  increases in the absence of dissolution. We also observe that the amount of trapped  $\text{CO}_2$  due to residual trapping remains unchanged once it reaches the maximum value (shown in Fig. 8B). This differs from what we have seen in the base case. It can be inferred that the convective transport driven by dissolution during the post-injection period leads to a shifting of constitutive relations, i.e., from scanning curves back to the primary drainage curve, in the region near sealing layer. As a result, the trapped gas turns into free gas and the trapped amount due to residual trapping decreases.

### 3.3. Role of capillary pressure

Intuitively, one would expect that exclusion of capillary pressure sharpens the  $\text{CO}_2$ -brine interfaces, which are observed in saturation profiles without capillary pressure — see Fig. 7C. In consequence, gas phase tends to have higher saturation values in the invading zone. This leads to a smaller swept area when injection ceases, resulting in reductions of dissolved  $\text{CO}_2$  compared to that of the base case. Moreover, such a reduction near the top layer undermines the convective transport in the post injection period: sinking fingers are less active compared with the base case. As shown in Fig. 8A, the amount of dissolved  $\text{CO}_2$

without capillarity starts to deviate from the base case after  $t \approx 0.1$ , and the deviation becomes more pronounced as time elapses.

The saturation profiles from the post injection period without capillarity (Fig. 7C) exhibit that gas saturation reaches its maximum value (0.8) in the layer underneath the top boundary. Consequently, a substantial amount of gas on the top layer is mobile, which may be subject to leakage from the cap rock. On the other hand, the maximum gas saturation in the base case throughout the process is 0.57, which is certainly smaller than 0.8. It can be inferred that capillary pressure helps the brine imbibe into the top layer, reverses the flow process before the saturation reaches its maximum value, and thus facilitates the residual trapping (Plug and Bruining, 2007; Wang and Tokunaga, 2015; Alyafei and Blunt, 2018). Fig. 8C shows that the amount of overall trapping in the absence of capillarity is reduced significantly compared to that of the base case.

### 3.4. Impact of absolute permeability

We have so far concentrated on the physics associated with fluids. In this subsection we study the impact of permeability on the trapping process. We first alter the absolute permeability in the homogeneous case, and then examine heterogeneous permeability fields.

#### 3.4.1. Homogeneous field

We consider two more permeability values, one is lower than that of the base, i.e.,  $k = 20\text{md}$ , and the other one is higher. Note that a higher permeability leads to an earlier breakthrough; to ensure all injected  $\text{CO}_2$  remains in the aquifer, we set the higher one to be  $k = 72\text{md}$ . Changing absolute permeability affects the relative significance of the viscous force and gravity force, as indicated by the gravity number,  $N_{gv}$ , which is proportional to the vertical permeability. In the homogeneous case, the permeability field is isotropic, i.e.,  $k_x = k_z = k$ , so that an aquifer with a lower  $k$  results in a smaller  $N_{gv}$ . A larger/smaller  $N_{gv}$  indicates the gravity/viscous force is more dominant, respectively. As shown in Fig. 10A, in the case of  $k = 72\text{md}$ , the  $\text{CO}_2$  plume forms a stronger gravity tongue compared to that of the base case: the displacement front has propagated to the right boundary when injection stops ( $t = 1$ ). This is because injected  $\text{CO}_2$  readily rises towards the top due to the predominant gravity force. On the contrary, Fig. 10B shows that for displacement with a low  $N_{gv}$ , gas saturation maps exhibit a distinct horizontal migration of the injected  $\text{CO}_2$ . In post-injection period, a higher  $k$  facilitates the gravity-induced convective transport thereby expediting the growth of sinking fingers.

The associated dynamic behavior of different trapping mechanisms are presented in Fig. 11. As shown in Fig. 11A, differences of the dissolved amount during the injection period are insignificant. Meanwhile, different values of  $k$  lead to different flow configurations which are clearly depicted in solution  $\text{CO}_2$ -brine ratio profiles. Note that during the injection period, most of the swept cells are in a saturated state: the solution  $\text{CO}_2$ -brine ratio profiles exhibit little variation in color. For this reason, each swept cell dissolves same amount of  $\text{CO}_2$  approximately, and the total dissolved amount could be estimated by the swept area. In view of the minor differences of fraction curves shown in Fig. 11A at  $t = 1$ , we can infer that at the end of injection, the swept areas in the studied cases of differing  $k$  are close.

Fig. 11B shows the fraction of residual trapping for the three investigated cases. A smaller  $k$  results in a larger trapped amount (maximum value) before decline occurs. This is due to the fact that in the case of low  $k$ , swept cells that participate in residual trapping have a higher free gas saturation prior to the cease of injection, and a higher free gas saturation is transitioned into a larger residual gas saturation following the linear trapping model. Moreover, the gravity-induced convective transport is suppressed in such a low  $k$  case. As a result, we observe that in the post-injection period, the decline for  $k = 20\text{md}$  is negligible, whereas the fraction curves obtained from the remaining two cases exhibit pronounced reductions. In the end, the residual trapping amount differs significantly, and it plays the major role in determining the overall trapped amount — see Fig. 11C.

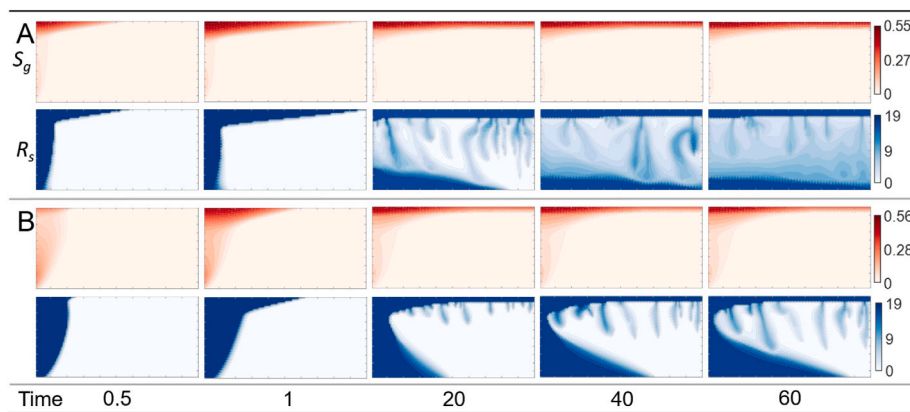


Fig. 10. Gas phase saturation and solution CO<sub>2</sub>-brine ratio profiles for two homogeneous permeability fields. (A) and (B) show results obtained from the case of  $k = 72\text{md}$  and  $k = 20\text{md}$ , respectively.

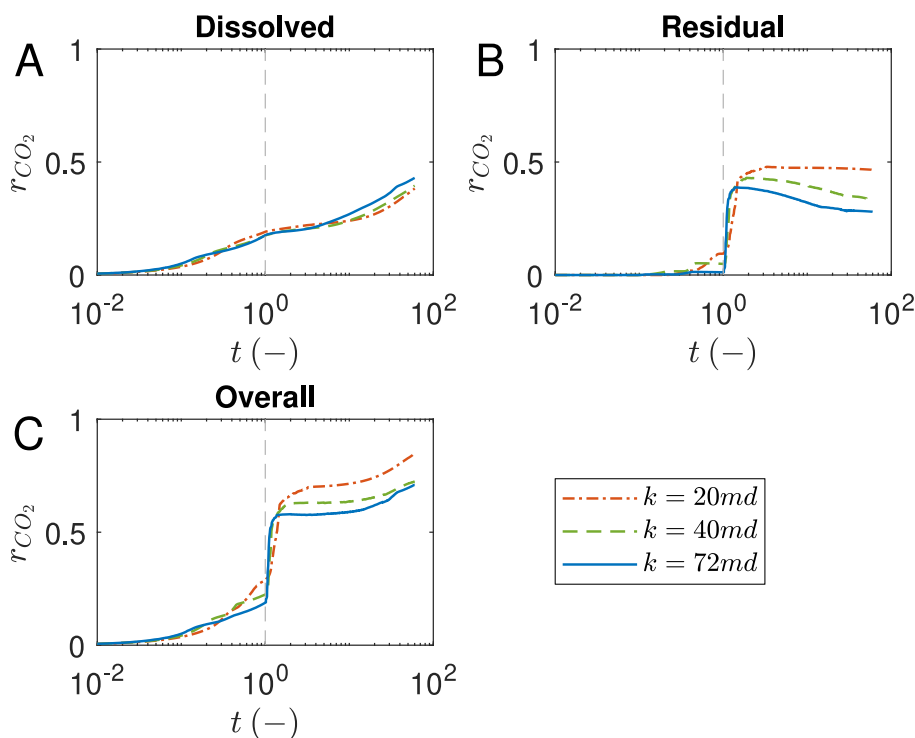


Fig. 11. Fraction of injected CO<sub>2</sub> trapped by different mechanisms in heterogeneous permeability fields. The vertical dashed line indicates the moment at which injection ceases ( $t = 1$ ).

### 3.4.2. Heterogeneous field

Here two heterogeneous permeability fields are investigated with varying spatial correlations. ‘mSPE10Top’ and ‘mSPE10Bottom’ exhibit patchy and channeling patterns, respectively. As shown in the gas phase saturation maps in Fig. 12, during the injection period, free CO<sub>2</sub> mainly accumulates in areas (a) underneath the top boundary, and (b) near the injection well. Such physical processes have been identified in the study of homogeneous fields. Similar to what we have seen in the case of  $k = 20\text{md}$  in which free CO<sub>2</sub> tends to migrate in the horizontal direction, here we observe that some CO<sub>2</sub> migrates laterally in the low permeability region near the injection well. Such movement is initiated by the viscous force which overwhelms the gravity forces locally. This lateral movement increases the swept area so that it benefits dissolution trapping. In addition, free gas accumulates in the low permeability region, and therefore, such movement favors residual trapping as well.

After the injection ceases, solution ratio maps in Figs. 12A and 12B show that the propagation of sinking fingers from the top saturated layer is impacted by the permeability distribution significantly.

Originated from different locations along the interface, these fingers tend to invade in high permeability zones, which results in complex configurations. In the end, the overall trapped amount in heterogeneous cases is greater than that in the base case — see Fig. 13C.

It is noted that another trapping mechanism, referred to as local capillary trapping, occurs when the buoyant CO<sub>2</sub> encounters a region in which the local capillary entry pressure is greater than the average pressure of gas phase. In this case CO<sub>2</sub> tends to accumulate or migrate beneath such a region (Saadatpoor et al., 2010; Jackson and Krevor, 2020). Here we assume a relatively negligible capillary entry pressure. As a result, this trapping mechanism is not accounted for in cases with heterogeneous permeability fields, which deserves future investigation.

## 4. Conclusions

We have systematically investigated CO<sub>2</sub> storage in saline aquifers in a full-cycle period via the recently developed unified numerical

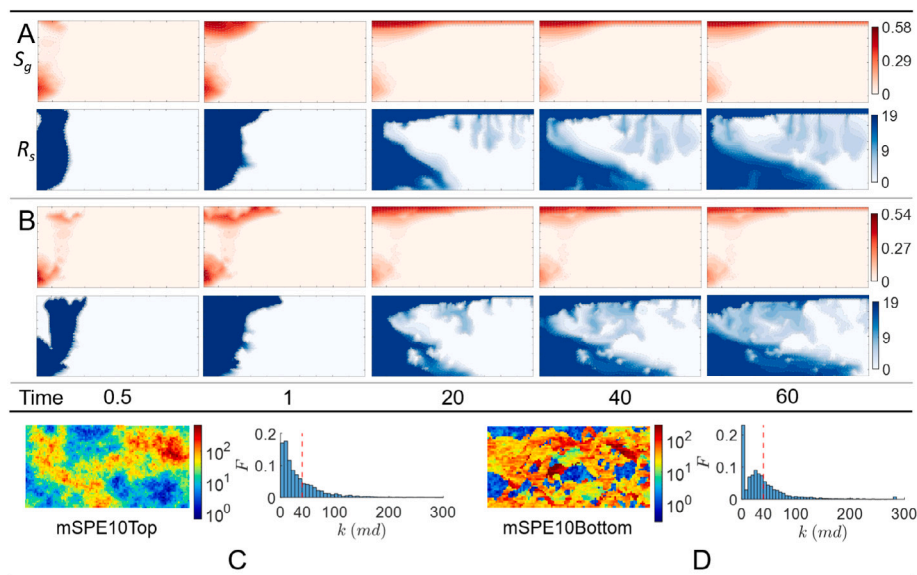


Fig. 12. Gas phase saturation and solution  $\text{CO}_2$ -brine ratio profiles for two in heterogeneous permeability fields. (A) and (B) present results from the permeability field given by 'mSPE10Top' and 'mSPE10Bottom', respectively. Spatial distribution of these two heterogeneous permeability maps, along with their histograms are shown in (C) and (D) in units of mD. In each histogram, the average value is indicated by a dashed line.

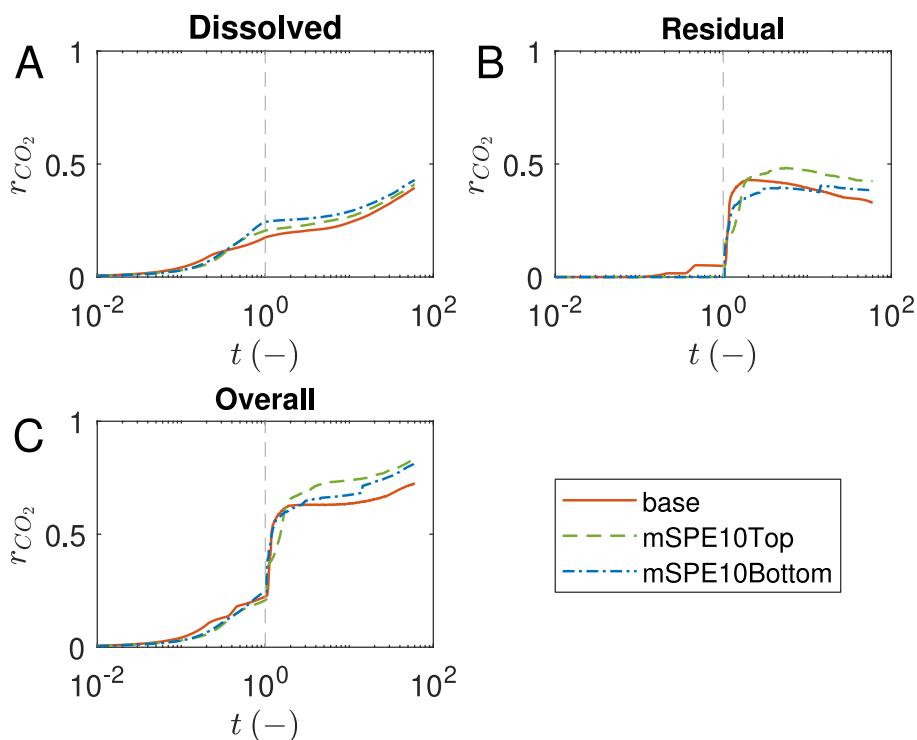


Fig. 13. Fraction of injected  $\text{CO}_2$  trapped by different mechanisms in heterogeneous permeability fields. The vertical dashed line indicates the moment at which injection ceases ( $t = 1$ ).

framework. Our Model represents the hysteretic characteristics of the constitutive relations, i.e., relative permeability and capillary pressure, in a robust manner. Moreover, we employ a compositional formulation to capture the dissolution trapping, in which the  $\text{CO}_2$ -brine ratio is calculated based on an accurate thermodynamic model.

Through visualization of saturation and solution ratio profiles at different stages, we have provided numerical evidence that the residual and dissolution trapping have their own time scales of importance. In particular, residual trapping comes into effect mainly after the injection ceases, whereas dissolution trapping has played a significant

role from the beginning of injection. Residual trapping is affected by the swept area in which flow processes will be reversed, and the associated free gas saturation when injection ceases. In post injection period, the convective transport triggered by the density difference due to dissolution trapping, reactivates a certain amount of immobile gas, resulting in a reduction of the trapped amount from residual trapping. Such a reduction becomes less pronounced in the case of a homogeneous aquifer with a lower permeability. Furthermore, we show that contribution from residual trapping regarding the overall trapped amount increases for a system with a lower permeability. Therefore,

it is critical to characterize the hysteresis behavior in such systems accurately.

On the other side, the solution CO<sub>2</sub>–brine ratio profiles reveal that the dissolution trapping operates under varying mechanisms at different stages. During injection period, dissolution occurs in the swept area. In this stage both trapping mechanisms are controlled by advective flow dynamics.

Different flow configurations due to differing driving forces may give comparable swept areas, and result in similar trapped amounts. The existence of spatial heterogeneity, i.e., heterogeneous permeability field, enlarges the swept area and therefore enhances the dissolution trapping. After injection ceases, dissolution continues across the subsequent interface via gravity-induced convective transport. The dissolution rate becomes relatively small because it takes time for the sinking fingers to generate and grow. After this transition period the rate has an observable increase indicating the sinking fingers have fully developed. These findings highlight the significance of capturing CO<sub>2</sub> plume migration during the early injection time, which is strongly connected to the assessment of trapped CO<sub>2</sub> in post injection period.

Our results reveal the inherent multiscale nature of CO<sub>2</sub> storage in saline aquifers. Understanding the interplay between different trapping mechanisms is essential for an accurate assessment of trapped CO<sub>2</sub> in a full cycle period. This study lays the foundation for interpretation of physical observations, optimal design of field operations, and further investigation of CO<sub>2</sub> storage in faulted and fractured systems.

#### CRediT authorship contribution statement

**Yuhang Wang:** Conceptualization, Methodology, Software, Writing – original draft. **Cornelis Vuik:** Writing – editing. **Hadi Hajibeygi:** Conceptualization, Methodology, writing – editing, Grant acquiring.

#### Declaration of competing interest

The authors declare that they have no known competing financial interests or personal relationships that could have appeared to influence the work reported in this paper.

#### Acknowledgments

Hadi Hajibeygi was sponsored by the Dutch National Science Foundation (NWO) under Vidi Talent Program Project “ADMIRE” (project number 17509). We thank the ADMIRE user committee for allowing us to publish this paper. Groups members of DARSIM (Delft Advanced Reservoir Simulation) and ADMIRE (Adaptive Dynamic Multiscale Integrated Reservoir Earth) are acknowledged for fruitful discussions during the development of this work. The source code developed for this research is openly accessible via <https://gitlab.com/darsim> address.

#### Appendix. Solubility of CO<sub>2</sub>

Here we present detailed workflow for calculating the solubility of CO<sub>2</sub> at given temperature and salinity. First we consider an equilibrium system which is composed of CO<sub>2</sub> and H<sub>2</sub>O. The equilibrium constants are given by

$$\kappa_{\text{H}_2\text{O}} = \frac{f_{\text{H}_2\text{O}(g)}}{a_{\text{H}_2\text{O}(l)}}, \quad (\text{A.1})$$

and

$$\kappa_{\text{CO}_2} = \frac{f_{\text{CO}_2(g)}}{a_{\text{CO}_2(l)}}, \quad (\text{A.2})$$

where  $a_c$  is the activity coefficient of component  $c$  in liquid phase,  $f_c$  is the fugacity of component  $c$  in gas phase defined as

$$f_c = \varphi_c x_{c,g} p, \quad (\text{A.3})$$

where  $\varphi_c$  is the fugacity coefficient and  $p$  is total pressure. The equilibrium constant at given temperature and pressure is expressed as (Spycher et al., 2003)

$$\kappa_c(T, p) = \kappa_c^0(T, p^0) \exp\left(\frac{(p - p^0) \bar{v}_c}{RT}\right), \quad (\text{A.4})$$

where  $R$  is gas constant,  $p^0$  is reference pressure (1 bar),  $\bar{V}_c$  is the average partial molar volume of the condensed component  $c$  over the pressure interval  $p^0$  to  $p$ . To calculate the mole fraction of CO<sub>2</sub> in liquid phase,  $x_{\text{CO}_2,l}$ , Eqs. (A.1) to (A.4) are recast by setting (Spycher et al., 2003)

$$A = \frac{\kappa_{\text{H}_2\text{O}}^0}{\varphi_{\text{H}_2\text{O}} p} \exp\left(\frac{(p - p^0) \bar{v}_{\text{H}_2\text{O}}}{RT}\right), \quad (\text{A.5})$$

and

$$B = \frac{\varphi_{\text{CO}_2} p}{55.508 \kappa_{\text{CO}_2}^0} \exp\left(-\frac{(p - p^0) \bar{v}_{\text{CO}_2}}{RT}\right), \quad (\text{A.6})$$

such that

$$x_{\text{CO}_2,l} = B \left(1 - x_{\text{H}_2\text{O},g}\right), \text{ where } x_{\text{H}_2\text{O},g} = \frac{1 - B}{1/A - B}. \quad (\text{A.7})$$

The fugacity coefficients in Eqs. (A.5) and (A.6) are derived using the Redlich–Kwong equation of state (RK-EOS) (Redlich and Kwong, 1949)

$$p = \frac{RT}{v - b} - \left(\frac{a}{T^{0.5} v(v + b)}\right), \quad (\text{A.8})$$

where  $v$  is molar volume,  $a$  and  $b$  are parameters associated with attractive and repulsive interactions, respectively. In the binary mixture system of H<sub>2</sub>O and CO<sub>2</sub>,  $a$  and  $b$  are calculated by the following mixing rules (Prausnitz et al., 1998)

$$a_m = x_{\text{H}_2\text{O},g}^2 a_{\text{H}_2\text{O}} + 2x_{\text{H}_2\text{O},g} x_{\text{CO}_2,g} a_{\text{H}_2\text{O}-\text{CO}_2} + x_{\text{CO}_2,g}^2 a_{\text{CO}_2}, \quad (\text{A.9})$$

and

$$b_m = x_{\text{H}_2\text{O},g} b_{\text{H}_2\text{O}} + x_{\text{CO}_2,g} b_{\text{CO}_2}. \quad (\text{A.10})$$

The fugacity coefficient of a component  $c$ ,  $\varphi_c$ , is then calculated based on these mixing rules and RK-EOS (Prausnitz et al., 1998)

$$\begin{aligned} \ln(\varphi_c) = & \ln\left(\frac{v}{v - b_m}\right) + \left(\frac{b_c}{v - b_m}\right) - \left(\frac{2 \sum_i^{n_c} x_{i,g} a_{ic}}{RT^{1.5} b_m}\right) \ln\left(\frac{v + b_m}{v}\right) \\ & + \left(\frac{a_m b_c}{RT^{1.5} b_m^2}\right) \left[\ln\left(\frac{v + b_m}{v}\right) - \left(\frac{b_m}{v + b_m}\right)\right] - \ln\left(\frac{pv}{RT}\right). \end{aligned} \quad (\text{A.11})$$

To facilitate the implementation, we assume CO<sub>2</sub> exists in both liquid and gas phases whereas H<sub>2</sub>O exists in liquid phase only. This assumption implies  $x_{\text{H}_2\text{O},g} = 0$  and  $x_{\text{CO}_2,g} = 1$ . As a result,  $a_m$  and  $b_m$  in Eqs. (A.9) and (A.10) are simplified to  $a_{\text{CO}_2}$  and  $b_{\text{CO}_2}$ , respectively. Now that  $x_{\text{CO}_2,l}$  is obtained, the CO<sub>2</sub> molality in H<sub>2</sub>O can be calculated given by

$$m_{\text{CO}_2}^0 = \frac{55.508 x_{\text{CO}_2,g}}{1 - x_{\text{CO}_2,g}}. \quad (\text{A.12})$$

we have focused on CO<sub>2</sub>–H<sub>2</sub>O mixtures so far; to connect CO<sub>2</sub> molality in pure water to that in brine, the CO<sub>2</sub> activity coefficient is used

$$m_{\text{CO}_2} = \frac{m_{\text{CO}_2}^0}{\gamma_{\text{CO}_2}}. \quad (\text{A.13})$$

Using the CO<sub>2</sub> molality in brine, the mole fraction of CO<sub>2</sub> in liquid phase can be calculated by

$$x_{\text{CO}_2,l} = \frac{m_{\text{CO}_2}}{m_{\text{CO}_2} + 55.508 + n_i m_s}, \quad (\text{A.14})$$

where  $n_i$  is the stoichiometric number of ions in the salt and  $m_s$  is salt molality. At last, the solution CO<sub>2</sub>-brine ratio is obtained by

$$R_s = \frac{\rho_b^{\text{STC}} x_{\text{CO}_2, l}}{\rho_{\text{CO}_2}^{\text{STC}} (1 - x_{\text{CO}_2, l})} \quad (\text{A.15})$$

Eq. (A.15) holds for cells in saturated state.

## References

- Abdoulghafour, H., Sarmadivaleh, M., Hauge, L.P., Fernø, M., Iglauer, S., 2020. Capillary pressure characteristics of CO<sub>2</sub>-brine-sandstone systems. *Int. J. Greenh. Gas Control* 94, 102876.
- Akbarabadi, M., Piri, M., 2013. Relative permeability hysteresis and capillary trapping characteristics of supercritical CO<sub>2</sub>/brine systems: An experimental study at reservoir conditions. *Adv. Water Resour.* 52, 190–206.
- Al-Khdheawi, E.A., Vialle, S., Barifcani, A., Sarmadivaleh, M., Iglauer, S., 2017. Impact of reservoir wettability and heterogeneity on CO<sub>2</sub>-plume migration and trapping capacity. *Int. J. Greenh. Gas Control* 58, 142–158.
- Alyafei, N., Blunt, M.J., 2018. Estimation of relative permeability and capillary pressure from mass imbibition experiments. *Adv. Water Resour.* 115, 88–94.
- Ampomah, W., Balch, R., Cather, M., Will, R., Gunda, D., Dai, Z., Soltanian, M., 2017. Optimum design of CO<sub>2</sub> storage and oil recovery under geological uncertainty. *Appl. Energy* 195, 80–92.
- Aziz, K., 1979. Petroleum reservoir simulation. *Appl. Sci. Publ.* 476.
- Bachmat, Y., Bear, J., 1964. The general equations of hydrodynamic dispersion in homogeneous, isotropic, porous mediums. *J. Geophys. Res.* 69 (12), 2561–2567.
- Bachu, S., 2015. Review of CO<sub>2</sub> storage efficiency in deep saline aquifers. *Int. J. Greenh. Gas Control* 40, 188–202.
- Bachu, S., Bonijoly, D., Bradshaw, J., Burruss, R., Holloway, S., Christensen, N.P., Mathiassen, O.M., 2007. CO<sub>2</sub> Storage capacity estimation: Methodology and gaps. *Int. J. Greenh. Gas Control* 1 (4), 430–443.
- Bachu, S., Gunter, W., Perkins, E., 1994. Aquifer disposal of CO<sub>2</sub>: hydrodynamic and mineral trapping. *Energy Convers. Manage.* 35 (4), 269–279.
- Bandilla, K.W., Celia, M.A., Birkholzer, J.T., Cihan, A., Leister, E.C., 2015. Multiphase modeling of geologic carbon sequestration in saline aquifers. *Groundwater* 53 (3), 362–377.
- Barenblatt, G., Patzek, T., Silin, D., 2002. The mathematical model of non-equilibrium effects in water-oil displacement. In: *SPE/DOE Improved Oil Recovery Symposium*. OnePetro.
- Battistelli, A., Calore, C., Pruess, K., 1997. The simulator TOUGH2/EWASG for modelling geothermal reservoirs with brines and non-condensable gas. *Geothermics* 26 (4), 437–464.
- Bear, J., 2013. *Dynamics of Fluids in Porous Media*. Courier Corporation.
- Berg, S., Ott, H., 2012. Stability of CO<sub>2</sub>-brine immiscible displacement. *Int. J. Greenh. Gas Control* 11, 188–203.
- Bui, M., Adjiman, C.S., Bardow, A., Anthony, E.J., Boston, A., Brown, S., Fennell, P.S., Fuss, S., Galindo, A., Hackett, L.A., et al., 2018. Carbon capture and storage (CCS): the way forward. *Energy Environ. Sci.* 11 (5), 1062–1176.
- Carlson, F.M., 1981. Simulation of relative permeability hysteresis to the nonwetting phase. In: *SPE Annual Technical Conference and Exhibition*. Society of Petroleum Engineers.
- Celia, M., Bachu, S., Nordbotten, J., Bandilla, K., 2015. Status of CO<sub>2</sub> storage in deep saline aquifers with emphasis on modeling approaches and practical simulations. *Water Resour. Res.* 51 (9), 6846–6892.
- Christie, M.A., Blunt, M., 2001. Tenth SPE comparative solution project: A comparison of upscaling techniques. In: *SPE Reservoir Simulation Symposium*. Society of Petroleum Engineers.
- Class, H., Ebigbo, A., Helmig, R., Dahle, H.K., Nordbotten, J.M., Celia, M.A., Audigane, P., Darcis, M., Ennis-King, J., Fan, Y., et al., 2009. A benchmark study on problems related to CO<sub>2</sub> storage in geologic formations. *Comput. Geosci.* 13 (4), 409–434.
- Court, B., Bandilla, K.W., Celia, M.A., Janzen, A., Dobossy, M., Nordbotten, J.M., 2012. Applicability of vertical-equilibrium and sharp-interface assumptions in CO<sub>2</sub> sequestration modeling. *Int. J. Greenh. Gas Control* 10, 134–147.
- Cusini, M., Fryer, B., van Kruijsdijk, C., Hajibeygi, H., 2018. Algebraic dynamic multilevel method for compositional flow in heterogeneous porous media. *J. Comput. Phys.* 354, 593–612.
- Dai, Z., Middleton, R., Viswanathan, H., Fessenden-Rahn, J., Bauman, J., Pawar, R., Lee, S.Y., McPherson, B., 2014. An integrated framework for optimizing CO<sub>2</sub> sequestration and enhanced oil recovery. *Environ. Sci. Technol. Lett.* 1 (1), 49–54.
- Dai, Z., Xu, L., Xiao, T., McPherson, B., Zhang, X., Zheng, L., Dong, S., Yang, Z., Soltanian, M.R., Yang, C., et al., 2020. Reactive chemical transport simulations of geologic carbon sequestration: Methods and applications. *Earth-Sci. Rev.* 103265.
- Danesh, A., 1998. *PVT and Phase Behaviour of Petroleum Reservoir Fluids*. Elsevier.
- De Paoli, M., 2021. Influence of reservoir properties on the dynamics of a migrating current of carbon dioxide. *Phys. Fluids* 33 (1), 016602.
- Deng, H., Stauffer, P.H., Dai, Z., Jiao, Z., Surdam, R.C., 2012. Simulation of industrial-scale CO<sub>2</sub> storage: Multi-scale heterogeneity and its impacts on storage capacity, injectivity and leakage. *Int. J. Greenh. Gas Control* 10, 397–418.
- Dentz, M., Icardi, M., Hidalgo, J.J., 2018. Mechanisms of dispersion in a porous medium. *J. Fluid Mech.* 841, 851–882.
- Dentz, M., Tartakovsky, D.M., 2009. Abrupt-interface solution for carbon dioxide injection into porous media. *Transp. Porous Media* 79 (1), 15–27.
- Diamond, L.W., Akinfiev, N.N., 2003. Solubility of CO<sub>2</sub> in water from -1.5 to 100 °C and from 0.1 to 100 MPa: evaluation of literature data and thermodynamic modelling. *Fluid Phase Equilib.* 208 (1–2), 265–290.
- Doughty, C., 2010. Investigation of CO<sub>2</sub> plume behavior for a large-scale pilot test of geologic carbon storage in a saline formation. *Transp. Porous Media* 82 (1), 49–76.
- Duan, Z., Sun, R., 2003. An improved model calculating CO<sub>2</sub> solubility in pure water and aqueous NaCl solutions from 273 to 533 K and from 0 to 2000 bar. *Chem. Geol.* 193 (3–4), 257–271.
- Elenius, M., Voskov, D., Tchelep, H., 2015. Interactions between gravity currents and convective dissolution. *Adv. Water Resour.* 83, 77–88.
- Enick, R.M., Klara, S.M., 1990. CO<sub>2</sub> Solubility in water and brine under reservoir conditions. *Chem. Eng. Commun.* 90 (1), 23–33.
- Ershadnia, R., Hajirezaie, S., Amooie, A., Wallace, C.D., Gershenzon, N.I., Hosseini, S.A., Sturmer, D.M., Ritzi, R.W., Soltanian, M.R., 2021. CO<sub>2</sub> Geological sequestration in multiscale heterogeneous aquifers: Effects of heterogeneity, connectivity, impurity, and hysteresis. *Adv. Water Resour.* 151, 103895.
- Espinoza, D.N., Santamarina, J.C., 2017. CO<sub>2</sub> Breakthrough—Caprock sealing efficiency and integrity for carbon geological storage. *Int. J. Greenh. Gas Control* 66, 218–229.
- Fu, X., Cueto-Felgueroso, L., Juanes, R., 2013. Pattern formation and coarsening dynamics in three-dimensional convective mixing in porous media. *Phil. Trans. R. Soc. A* 371 (2004), 20120355.
- Gasda, S.E., Nordbotten, J.M., Celia, M.A., 2009. Vertical equilibrium with sub-scale analytical methods for geological CO<sub>2</sub> sequestration. *Comput. Geosci.* 13 (4), 469.
- Gaus, I., 2010. Role and impact of CO<sub>2</sub>-rock interactions during CO<sub>2</sub> storage in sedimentary rocks. *Int. J. Greenh. Gas Control* 4 (1), 73–89.
- Gershenzon, N.I., Ritzi, R.W., Dominic, D.F., Mehnert, E., Okwen, R.T., 2017. Capillary trapping of CO<sub>2</sub> in heterogeneous reservoirs during the injection period. *Int. J. Greenh. Gas Control* 59, 13–23.
- Green, C.P., Ennis-King, J., 2014. Steady dissolution rate due to convective mixing in anisotropic porous media. *Adv. Water Resour.* 73, 65–73.
- Group, C.M., 2020. *GEM User Guide*. Computer Modelling Group Calgary.
- Gunter, W., Perkins, E., Hutcheon, I., 2000. Aquifer disposal of acid gases: modelling of water-rock reactions for trapping of acid wastes. *Appl. Geochem.* 15 (8), 1085–1095.
- Guo, F., Aryana, S.A., 2019. An experimental investigation of flow regimes in imbibition and drainage using a microfluidic platform. *Energies* 12 (7), 1390.
- Guo, B., Bandilla, K.W., Doster, F., Keilegavlen, E., Celia, M.A., 2014. A vertically integrated model with vertical dynamics for CO<sub>2</sub> storage. *Water Resour. Res.* 50 (8), 6269–6284.
- Hajibeygi, H., Tchelep, H.A., 2014. Compositional multiscale finite-volume formulation. *SPE J.* 19 (02), 316–326.
- Han, W.S., Kim, K.-Y., Esser, R.P., Park, E., McPherson, B.J., 2011. Sensitivity study of simulation parameters controlling CO<sub>2</sub> trapping mechanisms in saline formations. *Transp. Porous Media* 90 (3), 807–829.
- Hassanzadeh, S.M., Gray, W.G., 1993. Thermodynamic basis of capillary pressure in porous media. *Water Resour. Res.* 29 (10), 3389–3405.
- Hassanzadeh, H., Pooladi-Darvish, M., Elsharkawy, A.M., Keith, D.W., Leonenko, Y., 2008. Predicting PVT data for CO<sub>2</sub>-brine mixtures for black-oil simulation of CO<sub>2</sub> geological storage. *Int. J. Greenh. Gas Control* 2 (1), 65–77.
- Hassanzadeh, H., Pooladi-Darvish, M., Keith, D.W., 2007. Scaling behavior of convective mixing, with application to geological storage of CO<sub>2</sub>. *AIChE J.* 53 (5), 1121–1131.
- Hesse, M.A., Orr Jr., F., Tchelep, H., 2008. Gravity currents with residual trapping. *J. Fluid Mech.* 611, 35.
- Hewitt, D.R., Neufeld, J.A., Lister, J.R., 2013. Convective shutdown in a porous medium at high Rayleigh number. *J. Fluid Mech.* 719, 551–586.
- Hunt, J.R., Sitar, N., Udell, K.S., 1988. Nonaqueous phase liquid transport and cleanup: 1. analysis of mechanisms. *Water Resour. Res.* 24 (8), 1247–1258.
- Ide, S.T., Jessen, K., Orr Jr., F.M., 2007. Storage of CO<sub>2</sub> in saline aquifers: Effects of gravity, viscous, and capillary forces on amount and timing of trapping. *Int. J. Greenh. Gas Control* 1 (4), 481–491.
- Jackson, S.J., Krevor, S., 2020. Small-scale capillary heterogeneity linked to rapid plume migration during CO<sub>2</sub> storage. *Geophys. Res. Lett.* 47 (18), e2020GL088616.
- Jayne, R.S., Wu, H., Pollyea, R.M., 2019. Geologic CO<sub>2</sub> sequestration and permeability uncertainty in a highly heterogeneous reservoir. *Int. J. Greenh. Gas Control* 83, 128–139.
- Jiang, X., 2011. A review of physical modelling and numerical simulation of long-term geological storage of CO<sub>2</sub>. *Appl. Energy* 88 (11), 3557–3566.
- Joekar-Niasar, V., Hassanzadeh, S.M., Dahle, H., 2010. Non-equilibrium effects in capillarity and interfacial area in two-phase flow: dynamic pore-network modelling. *J. Fluid Mech.* 655, 38–71.
- Juanes, R., Spiteri, E., Orr Jr., F., Blunt, M., 2006. Impact of relative permeability hysteresis on geological CO<sub>2</sub> storage. *Water Resour. Res.* 42 (12).

- Killough, J., 1976. Reservoir simulation with history-dependent saturation functions. *Soc. Petroleum Eng. J.* 16 (01), 37–48.
- Kuo, C.W., Benson, S.M., 2015. Numerical and analytical study of effects of small scale heterogeneity on CO<sub>2</sub>/brine multiphase flow system in horizontal corefloods. *Adv. Water Resour.* 79, 1–17.
- Land, C.S., 1968. Calculation of imbibition relative permeability for two-and three-phase flow from rock properties. *Soc. Petroleum Eng. J.* 8 (02), 149–156.
- Lenormand, R., Touboul, E., Zarcone, C., 1988. Numerical models and experiments on immiscible displacements in porous media. *J. Fluid Mech.* 189, 165–187.
- Li, H., Jakobsen, J.P., Wilhelmsen, Ø., Yan, J., 2011a. PVTxy properties of CO<sub>2</sub> mixtures relevant for CO<sub>2</sub> capture, transport and storage: Review of available experimental data and theoretical models. *Appl. Energy* 88 (11), 3567–3579.
- Li, S., Zhang, Y., Zhang, X., 2011b. A study of conceptual model uncertainty in large-scale CO<sub>2</sub> storage simulation. *Water Resour. Res.* 47 (5).
- Liang, Y., Wen, B., Hesse, M.A., DiCarlo, D., 2018. Effect of dispersion on solutal convection in porous media. *Geophys. Res. Lett.* 45 (18), 9690–9698.
- Lyu, X., Voskov, D., Rossen, W.R., 2021. Numerical investigations of foam-assisted CO<sub>2</sub> storage in saline aquifers. *Int. J. Greenh. Gas Control* 108, 103314.
- MacMinn, C.W., Neufeld, J.A., Hesse, M.A., Huppert, H.E., 2012. Spreading and convective dissolution of carbon dioxide in vertically confined, horizontal aquifers. *Water Resour. Res.* 48 (11).
- Manceau, J.C., Rohmer, J., 2016. Post-injection trapping of mobile CO<sub>2</sub> in deep aquifers: Assessing the importance of model and parameter uncertainties. *Comput. Geosci.* 20 (6), 1251–1267.
- Matter, J.M., Kelemen, P.B., 2009. Permanent storage of carbon dioxide in geological reservoirs by mineral carbonation. *Nat. Geosci.* 2 (12), 837–841.
- Ni, H., Møyner, O., Kurtev, K.D., Benson, S.M., 2021. Quantifying CO<sub>2</sub> capillary heterogeneity trapping through macroscopic percolation simulation. *Adv. Water Resour.* 155, 103990.
- Nordbotten, J.M., Celia, M.A., Bachu, S., 2005. Injection and storage of CO<sub>2</sub> in deep saline aquifers: analytical solution for CO<sub>2</sub> plume evolution during injection. *Transp. Porous Media* 58 (3), 339–360.
- Nordbotten, J.M., Flemisch, B., Gasda, S., Nilsen, H., Fan, Y., Pickup, G.E., Wiese, B., Celia, M.A., Dahle, H., Eigestad, G., et al., 2012. Uncertainties in practical simulation of CO<sub>2</sub> storage. *Int. J. Greenh. Gas Control* 9, 234–242.
- Oak, M.J., Baker, L., Thomas, D., 1990. Three-phase relative permeability of Berea sandstone. *J. Pet. Technol.* 42 (08), 1–054.
- Oostrom, M., White, M., Porse, S., Krevor, S., Mathias, S., 2016. Comparison of relative permeability–saturation–capillary pressure models for simulation of reservoir CO<sub>2</sub> injection. *Int. J. Greenh. Gas Control* 45, 70–85.
- Orr Jr., F.M., 2009. CO<sub>2</sub> Capture and storage: Are we ready? *Energy Environ. Sci.* 2 (5), 449–458.
- Pini, R., Benson, S.M., 2017. Capillary pressure heterogeneity and hysteresis for the supercritical CO<sub>2</sub>/water system in a sandstone. *Adv. Water Resour.* 108, 277–292.
- Pirozzoli, S., De Paoli, M., Zonta, F., Soldati, A., 2021. Towards the ultimate regime in Rayleigh–Darcy convection. *J. Fluid Mech.* 911.
- Plohr, B., Marchesin, D., Bedrikovetsky, P., Krause, P., 2001. Modeling hysteresis in porous media flow via relaxation. *Comput. Geosci.* 5 (3), 225–256.
- Plug, W.J., Bruining, J., 2007. Capillary pressure for the sand–CO<sub>2</sub>–water system under various pressure conditions. Application to CO<sub>2</sub> sequestration. *Adv. Water Resour.* 30 (11), 2339–2353.
- Prausnitz, J.M., Lichtenthaler, R.N., De Azevedo, E.G., 1998. *Molecular Thermodynamics of Fluid-Phase Equilibria*. Pearson Education.
- Pruess, K., Oldenburg, C.M., Moridis, G., 1999. TOUGH2 User's Guide Version 2. Technical Report, Lawrence Berkeley National Lab.(LBNL), Berkeley, CA (United States).
- Randolph, J.B., Saar, M.O., 2011. Combining geothermal energy capture with geologic carbon dioxide sequestration. *Geophys. Res. Lett.* 38 (10), L10401.
- Rasmusson, K., Rasmusson, M., Tsang, Y., Niemi, A., 2016. A simulation study of the effect of trapping model, geological heterogeneity and injection strategies on CO<sub>2</sub> trapping. *Int. J. Greenh. Gas Control* 52, 52–72.
- Redlich, O., Kwong, J.N., 1949. On the thermodynamics of solutions. V. An equation of state. Fugacities of gaseous solutions. *Chem. Rev.* 44 (1), 233–244.
- Riaz, A., Tchelepi, H.A., 2006. Numerical simulation of immiscible two-phase flow in porous media. *Phys. Fluids* 18 (1), 014104.
- Rinaldi, A.P., Rutqvist, J., Cappa, F., 2014. Geomechanical effects on CO<sub>2</sub> leakage through fault zones during large-scale underground injection. *Int. J. Greenh. Gas Control* 20, 117–131.
- Rubin, E., De Coninck, H., 2005. IPCC special report on carbon dioxide capture and storage. UK: Camb. Univ. Press TNO (2004): Cost Curves CO<sub>2</sub> Storage, Part 2, 14.
- Ruprecht, C., Pini, R., Falta, R., Benson, S., Murdoch, L., 2014. Hysteretic trapping and relative permeability of CO<sub>2</sub> in sandstone at reservoir conditions. *Int. J. Greenh. Gas Control* 27, 15–27.
- Rutqvist, J., 2012. The geomechanics of CO<sub>2</sub> storage in deep sedimentary formations. *Geotech. Geol. Eng.* 30 (3), 525–551.
- Saadatpoor, E., Bryant, S.L., Sepehrnoori, K., 2010. New trapping mechanism in carbon sequestration. *Transp. Porous Media* 82 (1), 3–17.
- Saffman, P., 1959. A theory of dispersion in a porous medium. *J. Fluid Mech.* 6 (3), 321–349.
- Sathaye, K.J., Hesse, M.A., Cassidy, M., Stockli, D.F., 2014. Constraints on the magnitude and rate of CO<sub>2</sub> dissolution at bravo dome natural gas field. *Proc. Natl. Acad. Sci.* 111 (43), 15332–15337.
- Spycher, N., Pruess, K., 2005. CO<sub>2</sub>–H<sub>2</sub>O mixtures in the geological sequestration of CO<sub>2</sub>. II. Partitioning in chloride brines at 12–100 °C and up to 600 bar. *Geochim. Cosmochim. Acta* 69 (13), 3309–3320.
- Spycher, N., Pruess, K., Ennis-King, J., 2003. CO<sub>2</sub>–H<sub>2</sub>O mixtures in the geological sequestration of CO<sub>2</sub>. I. Assessment and calculation of mutual solubilities from 12 to 100 °C and up to 600 bar. *Geochim. Cosmochim. Acta* 67 (16), 3015–3031.
- Steffy, D., Barry, D., Johnston, C., 1997. Influence of antecedent moisture content on residual LNAPL saturation. *Soil Sediment Contam.* 6 (2), 113–147.
- Szulczewski, M.L., MacMinn, C.W., Herzog, H.J., Juanes, R., 2012. Lifetime of carbon capture and storage as a climate-change mitigation technology. *Proc. Natl. Acad. Sci.* 109 (14), 5185–5189.
- Tao, Y., Guo, B., Bandilla, K.W., Celia, M.A., 2019. Vertically integrated dual-continuum models for CO<sub>2</sub> injection in fractured geological formations. *Comput. Geosci.* 23 (2), 273–284.
- van Genuchten, M.T., 1980. A closed-form equation for predicting the hydraulic conductivity of unsaturated soils. *Soil Sci. Am. J.* 44 (5), 892–898.
- Voskov, D.V., Tchelepi, H.A., 2012. Comparison of nonlinear formulations for two-phase multi-component EoS based simulation. *J. Pet. Sci. Eng.* 82, 101–111.
- Wang, Y., Aryana, S.A., Allen, M.B., 2019. An extension of Darcy's law incorporating dynamic length scales. *Adv. Water Resour.* 129, 70–79.
- Wang, Y., Mckinzie, J., Furtado, F., Aryana, S.A., 2020. Scaling analysis of two-phase flow in fractal permeability fields. *Water Resour. Res.* 56 (11), e2020WR028214.
- Wang, S., Tokunaga, T.K., 2015. Capillary pressure–saturation relations for supercritical CO<sub>2</sub> and brine in limestone/dolomite sands: Implications for geologic carbon sequestration in carbonate reservoirs. *Environ. Sci. Technol.* 49 (12), 7208–7217.
- Wen, G., Benson, S.M., 2019. CO<sub>2</sub> plume migration and dissolution in layered reservoirs. *Int. J. Greenh. Gas Control* 87, 66–79.
- Wen, B., Chang, K.W., Hesse, M.A., 2018. Rayleigh–Darcy convection with hydrodynamic dispersion. *Phys. Rev. Fluids* 3 (12), 123801.
- White, J.A., Chiaramonte, L., Ezzedine, S., Foxall, W., Hao, Y., Ramirez, A., McNab, W., 2014. Geomechanical behavior of the reservoir and caprock system at the in salah CO<sub>2</sub> storage project. *Proc. Natl. Acad. Sci.* 111 (24), 8747–8752.
- Wriedt, J., Deo, M., Han, W.S., Lepinski, J., 2014. A methodology for quantifying risk and likelihood of failure for carbon dioxide injection into deep saline reservoirs. *Int. J. Greenh. Gas Control* 20, 196–211.
- Yamamoto, H., Doughty, C., 2011. Investigation of gridding effects for numerical simulations of CO<sub>2</sub> geologic sequestration. *Int. J. Greenh. Gas Control* 5 (4), 975–985.
- Yang, Z., Chen, Y.F., Niemi, A., 2020. Gas migration and residual trapping in bimodal heterogeneous media during geological storage of CO<sub>2</sub>. *Adv. Water Resour.* 142, 103608.
- Zappone, A., Rinaldi, A.P., Grab, M., Wenning, Q.C., Roques, C., Madonna, C., Obermann, A.C., Bernasconi, S.M., Brennwald, M.S., Kipfer, R., et al., 2021. Fault sealing and caprock integrity for CO<sub>2</sub> storage: an in situ injection experiment. *Solid Earth* 12 (2), 319–343.
- Zhang, C., Oostrom, M., Wietsma, T.W., Grate, J.W., Warner, M.G., 2011. Influence of viscous and capillary forces on immiscible fluid displacement: Pore-scale experimental study in a water-wet micromodel demonstrating viscous and capillary fingering. *Energy Fuels* 25 (8), 3493–3505.
- Zoback, M.D., Gorelick, S.M., 2012. Earthquake triggering and large-scale geologic storage of carbon dioxide. *Proc. Natl. Acad. Sci.* 109 (26), 10164–10168.